Brainstem neurons coordinate the bladder and urethra sphincter for urination

Xing Li[1], Xianping Li[2, 3], Jun Li[1], Han Qin[4], Shanshan Liang[2], Jun Li[2], Tingliang Jian[2], Xia Wang[5], Lingxuan Yin[1], Chunhui Yuan[3], Xiang Liao[5], Hongbo Jia[1, 6, 7]*, Xiaowei Chen[2, 4]*, Jiwei Yao[3, 5]*

[1]Advanced Institute for Brain and Intelligence, School of Physical Science and Technology, Guangxi University, Nanning, China.

[2]Brain Research Center and State Key Laboratory of Trauma and Chemical Poisoning, Third Military Medical University, Chongqing, China.

[3]Department of Urology, PLA Naval Medical Center, Naval Medical University, Shanghai, China.

[4]LFC Laboratory and Chongqing Institute for Brain and Intelligence, Guangyang Bay Laboratory, Chongqing, China.

[5]Center for Neurointelligence, School of Medicine, Chongqing University, Chongqing, China.

[6]Leibniz Institute for Neurobiology, Magdeburg, Germany.

[7]Suzhou Institute of Biomedical Engineering and Technology, Chinese Academy of Sciences, Suzhou, China.

*For correspondence: Hongbo Jia (jiahb@sibet.ac.cn), Xiaowei Chen (xiaowei_chen@tmmu.edu.cn), Jiwei Yao (jiwei_yao89@cqu.edu.cn)

Abstract

Urination, a vital and conserved process of emptying urine from the urinary bladder in mammals, requires precise coordination between the bladder and external urethra sphincter (EUS) that is tightly controlled by a complex neural network. However, the specific subpopulation of neurons that accounts for such coordination remains unidentified, limiting the development of target-specific therapies for certain urination disorders, e.g. detrusor-sphincter dyssynergia. Here, we find that cells expressing estrogen receptor 1 ($ESR1^{+}$) in the pontine micturition center (PMC) initiate voiding when activated and suspend ongoing voiding when suppressed, each at 100% reliability, respectively. Transection of either the pelvic or the pudendal nerve does not impair PMC^{ESR1+} control of the downstream target through the other nerve at all. Anatomically, PMC^{ESR1+} cells possess two subpopulations projecting to either the pelvic or pudendal nerve and a third, dual-projecting subpopulation, locking in the coordination of bladder contraction and sphincter relaxation in a rigid temporal order. We identify a cell type in the brainstem that controls the bladder-urethra coordination for urination.

Introduction

Urination is a basic life-maintaining function involving the coordinated control of two functional units of the lower urinary tract (Andersson and K.-E., 2004; Chang et al., 2018; Fowler et al., 2008), namely the bladder detrusor and external urethral sphincter (EUS). The coordination between the bladder and urethra sphincter for initiating or suspending voiding whenever needed should be executed at 100% reliability in healthy subjects. By contrast, impairment of such coordination (Cho et al., 2015; Taweel et al., 2015; Griffiths et al., 2005), at any rate, leads to various lower urinary tract dysfunctions (Sakakibara and Ryuji, 2015; Drake et al., 2014), significantly degrading the quality of life (Milsom et al., 2014; Aoki et al., 2017). While individual neural control pathways to either the bladder detrusor or the urethral sphincter have been extensively studied (Xiao et al., 2021; Lee et al., 2021), little is known about the neural mechanisms underlying their coordination, which impedes progress in developing target-specific therapies for certain urination disorders, such as detrusor-sphincter dyssynergia (DSD) (Stoffel, 2016; Seseke et al., 2019).

Individual neural pathways are present at different levels of the brain for the control of either the bladder or the EUS (Malykhina, 2017; Jin et al., 2020; Mukhopadhyay and Stowers,

53 2020). For example, at the cortical level, a subset of motor cortex neurons has been found to
54 drive bladder contraction through the projection to the brainstem (Yao et al., 2018). At the
55 brainstem level, the pontine micturition center (PMC; also referred to as Barrington's
56 nucleus) has long been considered a command hub region for urination control (Benarroch,
57 2010; Morrison, 2008). More recent studies have demonstrated that neurons expressing
58 corticotropin-releasing hormone (CRH) in the PMC (PMC^{CRH+}) control bladder contraction
59 (Hou et al., 2016; Ito et al., 2020), and neurons expressing estrogen receptor 1 (ESR1) in the
60 PMC (PMC^{ESR1+}) relax the sphincter (Keller et al., 2018), respectively. In addition, other
61 subcortical regions, including the periaqueductal gray (PAG) (Rao et al., 2022), lateral
62 hypothalamic area (LHA) (Verstegen et al., 2019; Hyun et al., 2021), and medial preoptic area
63 (MPOA) (Hou et al., 2016), have been suggested to play a potential role in urination control
64 by sending direct projections to the PMC. However, which brain areas coordinate both the
65 bladder and urethra sphincter remains unclear.
66 The most likely candidate region for coordinated control is the PMC. Neural tracing
67 experiments demonstrate that the PMC directly sends two bundles of glutamatergic axonal
68 projections, one to the sacral parasympathetic nucleus (SPN), where parasympathetic
69 bladder motoneurons are located, which send axons through the pelvic nerves for bladder
70 control; and the other one to the lumbosacral dorsal gray commissure (DGC) interneurons,
71 which inhibit the sphincter motoneurons in the dorsolateral nucleus (DL) for sphincter
72 control via the pudendal nerves (Kawatani et al., 2021; Jin et al., 2020). Early studies show
73 that microinjection of drugs into the PMC or electrical stimulation in the PMC causes bladder
74 contraction, sphincter relaxation, and urination (Mallory, 1991; Noto et al., 1989; Sugaya and
75 De Groat, 1994). However, the PMC consists of molecularly disparate cell subtypes
76 characterized by the expression of different marker genes, e.g. CRH positive cells (Ito et al.,
77 2020; Van Batavia et al., 2021), ESR1 positive cells (Vanderhorst et al., 2005), vesicular
78 glutamate transporter (Vglut2) and vesicular GABA transporter (VGAT) positive cells
79 (Verstegen et al., 2017; Hou et al., 2016). What remains unknown to date is which exact
80 neuronal subpopulation in the PMC accounts for such coordination of the bladder and
81 urethra sphincter. As previous anatomical results have shown that PMC^{CRH+} neurons mainly
82 project to the SPN in the spinal cord, whereas PMC^{ESR1+} neurons project to both the SPN and
83 DGC in the spinal cord (Keller et al., 2018; Kawatani et al., 2021), we hypothesize that
84 PMC^{ESR1+} cells could be a candidate for the coordination control and began our investigation.

85

Results

Voiding tightly correlates with PMC^{ESR1+} cell activity.

We performed fiber photometry monitoring of neuronal population Ca^{2+} activity (Rao et al., 2022) (fluorescence indicator: GCaMP6f) in the PMC of awake, unrestrained ESR1-Cre mice (Figure 1A and B, see Methods for detail). Each detected voiding event tightly correlated with a detected Ca^{2+} transient (Ca^{2+} transient preceding voiding by 0.7\0.3-0.9 s, median\25%-75% percentile, same notation hereinafter; n = 260 voiding events from 9 mice; Figure 1C and D), as verified by both an analysis of temporally shuffled data (peak Δf/f value, data: 31.8%\26.7%-33.2%; shuffled: 5.4%\3.7%-6.0%, n = 260 events of 9 mice, *p* = 3.9e-3, Wilcoxon signed-rank test; Figure 1E) and a blank control with an expression of inert fluorescence indicator, EYFP (Enhanced Yellow Fluorescent Protein), in PMC^{ESR1+} cells (detected voiding-associated fluorescence signal events: 100%\100% – 100%, n = 9 mice in test group; 0%\0% – 0%, n = 9 mice in control group, *p* = 4.1e-5, Wilcoxon rank-sum test; Figure 1F-figure supplement 1). To further test single-neuron correlates of voiding, we performed an 'opto-tagging' experiment (Qin et al., 2022) with a tetrode-fiber bundle implanted in the PMC of ESR1-Cre mice injected with AAV2/8-DIO-ChR2-mCherry (Figure 1G; see Methods for detail). Single PMC^{ESR1+} units were sorted and tagged by detecting reliable spikes to brief optical stimulation (e.g., latency: 4.04\3.02-4.6 ms, success rate: 97.5%\91.5%-100%; Figure supplement 2). The baseline-corrected firing rate of PMC^{ESR1+} units significantly exceeded that of non-PMC^{ESR1+} units in the temporal association window with voiding (PMC^{ESR1+} units: 'before', 0.04\-0.5-0.5 Hz, 'voiding', 1.4\-2.5e-11-3.8 Hz, n = 28 cells, *p* = 0.004; non-PMC^{ESR1+} units: 'before', 0.8\0.2-1.5 Hz, 'voiding', 1\-0.9-1.9 Hz, n = 51 cells, *p* = 0.6; Wilcoxon signed-rank test; Figure 1H and I). These results suggest that PMC^{ESR1+} cells' firing activities are tightly associated with voiding.

Additionally, we performed a set of combined physiological monitoring experiments, integrating fiber photometry, cystometry, and electromyography (EMG) of external urethral sphincter (EUS) simultaneously in urethane-anesthetized mice (Figure supplement 3A**,** see methods for detail). For quantitative measurement, we applied cystometry by continuously infusing saline into the bladder through a microcatheter (30-50 µl/min) to induce regular reflective voiding. A triple correlation of events was routinely observed, i.e., PMC^{ESR1+} neuronal activity, bladder pressure elevation, and the bursting pattern of EUS-EMG driving sphincter relaxation (Figure supplement 3B and C). This result was further validated by shuffled data analysis (Figure supplement 3D and E), demonstrating the robustness and

time-locking precision of the triple correlation events. However, it is important to note that the association between PMC^{ESR1+} cell activity and voiding in the other way around was not always 100%, i.e., for each detected Ca^{2+} transient, there could be either a voiding contraction (VC) or occasionally a non-voiding contraction (NVC) (Biallosterski et al., 2011) (27.1% of all detected events were in such case; Figure supplement 4A-C). Nevertheless, not only was the peak of bladder pressure lower, but also the amplitude of the photometry Ca^{2+} transient, which is known as a reliable report of collective neuronal population activity level, was significantly lower in NVC events than in VC events (NVCs: 8.8%\6.6%-14.7%, n = 62 events from 3 mice; VC: 15.01%\10.3%-26.4%, n = 167 events from 3 mice, p = 6.8e-9, Wilcoxon rank-sum test; figure supplement 4D and E), suggesting that not only the timing but also the strength of PMC^{ESR1+} cell activities were tightly correlated with successful voiding.

PMC^{ESR1+} cells bidirectionally operate the bladder and sphincter to initiate or suspend voiding.

With the tight correlation established, we moved on to test the causal relation between PMC^{ESR1+} cell activity and voiding. We started with a 'loss-of-function' test in awake mice, i.e., acute photoinhibition of PMC^{ESR1+} cells in a closed-loop to trigger the photoinhibition light as soon as the first patch of urine visualized (Figure 2A-figure supplement 5A; see Methods for detail). This test was also accompanied by a blank control in which all experimental conditions were the same except that the inhibitory opsin GtACR1 was absent. In photoinhibition events but not in the blank control events, the urine spot area was significantly reduced ('Pre': 34.1\27.1-40.4 cm^2; 'On': 9.9\7.9-11.1 cm^2, n = 12 mice in test group, p = 4.9e-4; 'Pre': 35.2\27.9-43.9 cm^2; 'On': 38.9\29.98-43.6 cm^2, n = 8 mice in control group, p = 0.3; Wilcoxon signed-rank test; Figure 2B and C), and the urination duration was significantly reduced as well ('Pre': 5.6\5.1-6.6 s; 'On': 1.38\1.19-1.42 s, p = 4.9e-4, Wilcoxon signed-rank test; Figure 2D and E). Effectively, the ongoing urination was fully suspended after a latency of 0.3 ± 0.1 sec from the onset of photoinhibition (Figure supplement 5B). To understand the physiological process during photoinhibition of PMC^{ESR1+} cells, we performed a simultaneous recording by measuring both the bladder pressure and the electromyograph of the external urethral sphincter (EUS-EMG) under urethane anesthesia (Figure 2F; see Methods for detail). This experiment also involved a closed-loop operation to trigger the light when observing the onset of the phasic bursting activity of the EUS-EMG that is known

151 to be directly associated with successful voiding in rodents (Kadekawa et al., 2016a; Langdale
152 and Grill, 2016). The maximum relative change in bladder pressure (ΔPressure) upon voiding
153 event was significantly reduced during photoinhibition compared to pre-inhibition baseline
154 events ('Pre': 11.6\10.4-15.4 cm H_2O, 'On': 8.1\5.9-9.4 cm H_2O, n = 8 mice, *p* = 7.8e-3,
155 Wilcoxon signed-rank test), but no such reduction was observed in the blank control group
156 ('Pre': 10.7\6.9-12.03 cm H_2O, 'On': 10.5\7.2-13.4 cm H_2O, n = 7 mice, *p* = 0.2, Wilcoxon
157 signed-rank test; Figure 2G and H). In the meanwhile, photoinhibition of the PMC^{ESR1+} cells
158 also halted the voiding-associated, phasic bursting activity of EMG, effectively reducing the
159 sphincter bursting duration ('Pre': 4.1\3.2-4.9 s, 'On': 0.98\0.9-1.2 s, *p* = 7.8e-3, Wilcoxon
160 signed-rank test; Figure 2G and I) at a latency of 0.1 ± 0.02 sec (Figure supplement 5C and D),
161 but no such effect was observed in the blank control group ('Pre': 3.3\2.9-4.8 s, 'On':
162 3.4\2.96-5.4 s, *p* = 0.8, Wilcoxon signed-rank test). Furthermore, the immediate suspension
163 of an ongoing voiding event by photoinhibition of PMC^{ESR1+} cells resulted in an expected side
164 effect that the threshold of bladder pressure to initiate the next voiding event (post-
165 photoinhibition) became higher (figure supplement 5E). A control test for the above set of
166 'loss-of-function' experiments was to test whether shorter durations of photoinhibition also
167 had the same urination suspension effect. To address this, we performed additional sets of
168 control experiments in which a shorter duration of photoinhibition (5 s light-on, instead of 60
169 s) resulted in the same, 100% suspension effect (Figure supplement 6). These data together
170 reveal that the acute photoinhibition of PMC^{ESR1+} cells halted both bladder contraction and
171 sphincter relaxation, thereby leading to a full suspension of the ongoing voiding process.
172 Then, we performed a 'gain-of-function' test in awake mice, i.e., acute photoactivation
173 of PMC^{ESR1+} cells that expressed the excitatory opsin channelrhodopsin-2 (ChR2), in a semi-
174 closed loop to trigger the light on when the bladder was filled to a level that was lower than
175 the threshold required for spontaneous voiding reflex (light on at 3.1 ± 0.03 min after the
176 previous voiding; inter-voiding interval under control condition: 6.6 ± 0.5 min; Figure 3A; see
177 Methods for detail). This test was also accompanied by a blank control in the absence of
178 ChR2. Light stimulation initiated voiding event at 100% reliability (100%\100%-100%, n = 172
179 trials of 8 mice; Figure 3B and C) in the test group (response latency, 0.7\0.6-0.8 s; Figure
180 3D), but almost 0% (0%\0%-1.25%, n = 166 trials of 8 mice) in the blank control group (Figure
181 3B and C). Accordingly, we also performed simultaneous cystometry with the EUS-EMG
182 experiment under urethane anesthesia (Figure 3E; see Methods for detail). Light stimulation
183 induced a prominent upstroke of bladder pressure in the test group and did not affect

184 bladder pressure at all in the control group (ΔP: 5.6\4.5-8.2 cm H_2O, n = 9 mice in the test
185 group, -0.1\-0.2-0.1 cm H_2O, n = 6 mice in the control group, p = 4e-4, Wilcoxon rank-sum
186 test; Figure 3F-H). Meanwhile, light stimulation triggered the phasic bursting activity of EUS-
187 EMG, at a success rate of 100% in the test group and nearly 0% in the control group (Figure
188 3F-H). An additional set of control experiments by using regular inter-stimulation intervals (5
189 s light-on per every 30 s) instead of the threshold-adaptive interval, yielded the same 100%
190 success rate of both bladder pressure and EUS-EMG responses (Figure supplement 7). Thus,
191 photoactivation of PMC^{ESR1+} cells resulted in initiating the voiding process through both
192 contracting the bladder and relaxing the sphincter. These sets of 'loss-of-function' and 'gain-
193 of-function' experiments together demonstrate that PMC^{ESR1+} cells perform as a 100%
194 reliable 'master switch' for either initiate or suspend voiding, provided that all downstream
195 targets are directly controlled and operational, which will be tested next.

196 **Transection of either the pudendal or pelvic nerve does not impair PMC^{ESR1+} neuronal**
197 **control of the other.**

198 To further confirm whether the effect of PMC^{ESR1+} cells on the bladder can occur
199 independently of sphincter relaxation, we designed a new set of simultaneous cystometry
200 and EUS-EMG experiments with $PMC^{ESR1\text{-}ChR2}$ mice subjected to first a pudendal nerve
201 transection (PDNx, disrupting the pathway from the PMC to the EUS) and then additionally a
202 pelvic nerve transection (PLNx, disrupting the pathway from the PMC to the bladder) in the
203 same mice under urethane anesthesia (Figure 4A; see Methods for detail). Under PDNx
204 condition, PMC^{ESR1+} cell photoactivation could not elicit EUS-EMG response at all, but
205 robustly elicited bladder pressure upstroke which was then fully abolished after PLNx (Figure
206 4B-E). Notably, the photoactivation-induced bladder pressure upstroke under the PDNx
207 condition was nearly the same as that in the pre-transection control condition (Figure 4D),
208 suggesting that the PMC^{ESR1+} cell control of the bladder was fully operational even when the
209 pudendal nerve to sphincter was severed.

210 Given that reflex signals from bladder afferents can indirectly influence the urethral
211 sphincter activity (Chang et al., 2007), we next investigated whether activation of PMC^{ESR1+}
212 cells directly induces the bursting pattern of EUS in the absence of bladder contraction. To
213 this end, the sequential nerve transection test was performed again with another group of
214 $PMC^{ESR1\text{-}ChR2}$ mice in a different order, i.e., first PLNx to disrupt the bladder nerve and then
215 PDNx to additionally disrupt the urethral sphincter nerve (Figure 5A; see Methods for detail).
216 Interestingly, under the PLNx condition with a filled bladder, PMC^{ESR1+} cell photoactivation did

217 not induce a bladder pressure upstroke (Δpressure: 3.2\0.96-4.9 cm H_2O in pre-transection
218 control condition, -1.2\-1.4- -0.8 cm H_2O in PLNx condition, n = 8 mice, *p* = 7.8e-3, Wilcoxon
219 signed-rank test), but the EUS-EMG activity remained responsive, leading to urine leakage
220 which consistently reduced bladder pressure (Figure 5B-E). Both the inversed bladder
221 response and the EUS-EMG response were then fully abolished after the second transection,
222 PDNx (Figure 5B-E-figure supplement 8). Consistently, under the PLNx condition with an
223 unfilled bladder, the EUS-EMG response was present, and the bladder pressure did not
224 change upon PMC^{ESR1+} cell photoactivation (Figure supplement 8). Collectively, these data
225 together indicate that PMC^{ESR1+} cell control of the urethra sphincter was operational even
226 when the pelvic nerve to the bladder was severed.

227 Lastly, despite that the PMC^{ESR1+} cell photoactivation consistently elicited EUS-EMG
228 bursting in 100% of cases, a refined analysis revealed that the key parameters of the
229 sphincter were slightly degraded under PLNx condition (EMG bursting AUC area: 0.21\0.20-
230 0.22 mV^*s in pre-transection, 0.17\0.15-0.19 mV^*s in PLNx; EMG bursting duration: 4.9\4.8-
231 5.03 s in pre-transection, 4.5\4.1-4.6 s in PLNx, n = 8 mice, *p* = 7.8e-3; Wilcoxon signed-rank
232 test; Figure 5E), which implies a potential reduction in effective voiding volume (Langdale
233 and Grill, 2016). To further explore this, we conducted experiments on awake, unrestrained
234 mice under the PLNx condition (Figure 6A**,** see Methods for detail). Compared to the pre-
235 transection control condition ('baseline'), PMC^{ESR1+} cell photoactivation still triggered voiding
236 in 100% of trials (Figure 6B and C). However, in PLNx mice, the voiding events were
237 characterized by significantly smaller urine spots and a longer latency to voiding onset than
238 the control events before transection, a difference not observed in the sham surgery group
239 (Figure 6D and E). These findings could be interpreted as that while the PMC^{ESR1+}-EUS
240 pathway is sufficient to drive voiding, as previously reported (Keller et al., 2018), however,
241 without an intact bladder reflex pathway involved, an efficient urine flow cannot be
242 performed. Piecing these data of the combined transection-optogenetics experiments
243 together, we reveal a more complete picture that PMC^{ESR1+} cells can operate the bladder
244 (through the pelvic nerve) and the sphincter (through the pudendal nerve) independently of
245 each other. Such refined knowledge could not have been obtained from simpler tests using
246 optogenetics alone as shown above (Figures 2 and 3), or from other experiments in the
247 literature (Hou et al., 2016; Keller et al., 2018; Ito et al., 2020).

248 **PMC^{ESR1+} cells coordinate bladder contraction and sphincter relaxation to initiate urination.**
249 The above data showing that PMC^{ESR1+} cells can operate through both the bladder and

urethral sphincter independently of each other implies that there should be two distinct anatomical projections from PMC^{ESR1+} cells downstream to innervate these targets. Indeed, our anterograde labeling experiment in ESR1-Cre mice (Figure supplement 9; see Methods for detail) showed that the mGFP-labelled axonal terminals of the PMC^{ESR1+} cell population were found in both the DGC and the SPN region of the lumbosacral spinal cord, which further send axons via the pudendal and pelvic nerves to innervate urethral sphincter and bladder, respectively. To further test this hypothesis, we performed retrograde labeling experiments in ESR1-Cre mice and, as a control, in CRH-Cre mice (Figure 7A and E; see Methods for detail). Analysis of CRH-Cre mice showed that 82.4% (80.1%\78.7%-86.7%) of PMC^{CRH+} cells were SPN-projecting only (expressing mCherry), and 1.8% (1.4%\1.1%-2.2%) were DGC-projecting only (expressing EGFP), whereas the remaining 15.8% (16.8%\11.4%-19.1%) were dual-projecting (altogether n = 1416 cells pooled from 79 slices obtained from 3 mice; Figure 7B-D). This result is consistent with the literature (Valentino et al., 2010; Ito et al., 2020; Hou et al., 2016; Keller et al., 2018) that PMC^{CRH+} cells primarily project to the SPN in the spinal cord and modulate bladder contraction. By contrast, analysis of the ESR1-Cre mice showed that 19.2% (24.1%\13.9%-24.2%) of PMC^{ESR1+} cells were SPN-projecting only, 53.3% (50.9%\41.2%-55.2%) were DGC-projecting only, and 27.5% (26.8%\25%-30.9%) cells were dual-projecting (n = 1417 cells pooled from 82 slices obtained from 5 mice; Figure 7F-H). These data suggest that PMC^{ESR1+} cells innervate either SPN or DGC in a more balanced manner and include a significant fraction of dual-innervating cells, in contrast to PMC^{CRH+} cells that primarily innervate the SPN.

The functional and anatomical data above together suggest that PMC^{ESR1+} cells can function as a 100% reliable 'master switch' either to initiate or to suspend voiding through independently operating the bladder (via SPN to the pelvic nerve) and the sphincter (via DGC to the pudendal nerve). We now come to the final question as to whether PMC^{ESR1+} cells can implement the coordination between the bladder and urethra sphincter, i.e., operate them in a rigid temporal order. We took advantage of the simultaneous recording of cystometry and EUS-EMG condition (e.g. Figure 2) in which the beginning/ending timepoint of bladder pressure upstroke (a significant rapid, transient increase in bladder pressure preceding voiding, denoting threshold pressure of bladder contraction) (Rana et al., 2024) and the stereotypic voiding-associated firing pattern of EUS-EMG (denoting sphincter relaxation) could be precisely determined. In the photometry recording experiments when voiding events spontaneously occurred, the bladder pressure upstroke timepoint always preceded the beginning timepoint of the EUS-EMG firing pattern (bladder pressure upstroke onset:

284 0.6\0.3-1.2 s, EMG bursting onset: 2.3\1.5-3.2 s, relative to the onset of Ca^{2+} signals; n = 46
285 events pooled from 8 mice; Figure 8A). Accordingly, in the photoactivation experiments, the
286 bladder pressure upstroke timepoint also preceded the EMG bursting pattern begin
287 timepoint, albeit both were slightly earlier than those in 'passive' spontaneous photometry
288 recordings (bladder pressure upstroke onset: 0.4\0.4-0.5 s, EMG bursting onset: 0.8\0.7-1.0
289 s; n = 50 events pooled from 10 mice; Figure 8B). Despite that the photoactivation of the
290 PMC^{ESR1+} cells could have been artificially strong and did not necessarily mimic the
291 naturalistic firing pattern of PMC^{ESR1+} cells (see Figure 1G-I), the same temporal order as
292 bladder contraction preceded sphincter relaxation suggests that the downstream circuity
293 was instructed to execute in the same temporal order. Intriguingly, in photoinhibition
294 experiments, the EMG pattern almost instantaneously ended, while the bladder pressure
295 upstroke end timepoint occurred later (EMG bursting end: 0.1\0.1-0.2 s; bladder pressure
296 upstroke end: 0.8\0.8-0.9 s, n = 44 events pooled from 8 mice; Figure 8C). These timing
297 results can be interpreted from a broader perspective by considering the lower spinal reflex
298 circuit together with PMC^{ESR1+} projections from the brainstem (Figure 8D). Since the lower
299 spinal reflex circuit is the forefront agent that can send a feedforward reflex signal from the
300 bladder to the sphincter unidirectionally (Lee et al., 2021; de Groat et al., 2015; Chang et al.,
301 2007; Abud et al., 2015), the brainstem coordination signal descending in two parallel paths
302 from PMC^{ESR1+} cells would result in the initiation of voiding with the same forwarding order
303 but in the suspension of ongoing voiding with the reversed order.

304 **Discussion**

305 A prominent aspect of our data is that voiding events 100% correlated with PMC^{ESR1+}
306 neuronal activity (Figure 1), and both photoactivation and photoinhibition of PMC^{ESR1+} cells
307 yielded a 100% success rate in initiating and suspending the process of voiding, respectively
308 (Figure 2 and 3). Whilst there are many other factors from both the lower spinal circuit and
309 the higher cortical/subcortical circuits together to determine in what condition to void (Yao
310 et al., 2018; de Groat et al., 2015; Sartori et al., 2022; de Groat, 2009; Zderic, 2019;
311 Mukhopadhyay and Stowers, 2020), the instantaneous execution to efficiently initiate or
312 suspend a voiding process involves a significant contribution of PMC^{ESR1+} cells in the
313 brainstem as demonstrated here in this study. The bidirectional control, i.e., in the one way
314 to initiate voiding whenever needed and suitable (which is a basic life need) (Mukhopadhyay
315 and Stowers, 2020), and in the other way to suspend an ongoing voiding when needed (e.g.,
316 to release only a small volume of urine for landmarking) (Keller et al., 2018; Hyun et al.,

317 2021; Desjardins et al., 1973), can be executed at 100% reliability by PMC^{ESR1+} cells given that
318 all downstream nerves and muscles are intact and operational.
319 Moreover, the anatomical data also revealed a significant fraction of dual-projecting
320 PMC^{ESR1+} cells (Figure 7H) which we consider to play a significant role in the coordination of
321 the bladder and sphincter. Because these two projections originate from the same cells, the
322 'on' and 'off' commands for bladder contraction sent from these cells would always align
323 with the 'on' and 'off' commands for sphincter relaxation, respectively. As such, the
324 brainstem can serve the upstream higher brain regions (Yao et al., 2018; Zare et al., 2019;
325 Manohar et al., 2017) (e.g., the neocortex) with a 100% reliable 'master switch' to urinate a
326 desired volume whenever in physiological or social needs (Mukhopadhyay and Stowers,
327 2020; Malykhina, 2017; Kaur et al., 2014), e.g., to mark territories with small urine spots as
328 an animal, or to urinate into a small sample tube for a health check as a human.
329 The fact that PMC^{ESR1+} cells can execute dynamic, real-time control of voiding at 100%
330 reliability does not imply that other cell types in the PMC are not required to achieve the
331 same goal of perfect urination control. On the contrary, we suggest that a proper baseline
332 control of bladder pressure is also mandatory, e.g., by CRH^{+} cells which are the majority of
333 cells in PMC that primarily operate the bladder through the pelvic nerve and can be
334 modulated by various contextual factors (Hou et al., 2016; Vincent and Satoh, 1984; Wood et
335 al., 2009). After all, it is not the cell type domain marker ESR1 (which by itself abundantly
336 expressed in many other regions of the brain and is involved in many other physiological and
337 cognitive functions (Karigo et al., 2021; Liu et al., 2022; Fang et al., 2018)), but rather the
338 topology of innervation (Figure 8D) that directly enables such a role of urination
339 coordination, i.e., a cell of whichever marker that locates in this particular brainstem nucleus
340 (PMC) (Kawatani et al., 2021) and possesses dual innervations towards both the bladder and
341 sphincter is a potent contributor to urination coordination (Griffiths, 2015). Nevertheless,
342 our pinpointing of PMC^{ESR1+} cells performing a 100% reliable role in bladder-sphincter
343 coordination enlightens the future development of precise therapies for treating urination
344 coordination disorders.

345 **Conclusions**

346 In summary, we have identified the essential role of PMC^{ESR1} neurons in coordinating
347 urination through co-innervation of both the bladder and urethra sphincter. Our findings
348 offer new insights into the anatomical and physiological basis and research paradigms for the
349 coordinated engagement of parasympathetic and somatic functions of urination control.

350 PMC^{ESR1} neurons may serve as a key focal point for advancing our understanding of the
351 neural mechanisms underlying urination, both in physiological contexts and pathological
352 conditions such as brain injuries, spinal cord injuries, and peripheral nerve damages.

353

354 **Materials and Methods**

355 **Animals**

356 The experiment procedures were approved by the Third Military Medical University Animal
357 Care and Use Committee and were conducted strictly in adherence to established guidelines.
358 This study utilized ESR1-IRES-Cre (Jackson Laboratory, stock #017911) (Lee et al., 2014) and
359 CRH-IRES-Cre (Jackson Laboratory, stock #012704) (Baram et al., 2015) mice. These mice
360 were group-housed in an environment-controlled room at 23-25℃ and 50% humidity, with 4-
361 5 mice per cage, on a 12-hour light/dark cycle, and with free access to food and water. Mice
362 implanted with optical fibers were housed individually. Both male and female mice, aged 8-
363 20 weeks, were randomly assigned to various experiments. The figure legends and
364 supplement tables detail the number of animals utilized in each experiment.

365 **Virus vectors and CTB**

366 The study utilized the following viruses and cholera toxin subunit B (CTB) for various
367 experiments: For fiber photometry recording experiments, AAV2/9-DIO-GCaMP6f (titer: 0.5 ×
368 10^{12} vg/ml) was unilaterally injected into the PMC. For optogenetic manipulation
369 experiments, AAV2/9-hsyn-DIO-hGtACR1-mCherry (titer: 1.43 × 10^{13} vg/ml) and AAV2/8-DIO-
370 ChR2-mCherry (titer: 1.33 × 10^{13} vg/ml) were bilaterally delivered into the PMC for
371 photoinhibition and photoactivation, respectively. For retrograde tracing experiments,
372 pAAV2/retro-EF1a-DIO-EGFP (titer: ≥ 1.00 × 10^{12} vg/ml) and pAAV2/retro-EF1a-DIO-mCherry
373 (titer: ≥1.00 × 10^{12} vg/ml) were injected into the spinal cords of ESR1-Cre and CRH-Cre mice,
374 respectively. For anterograde tracing experiments, AAV2/9-hEF1a-fDIO-mGFP (titer: 1.00 ×
375 10^{13} vg/ml) was injected unilaterally into the PMC, and a 10: 1 volume mixture of
376 AAV2/2Retro-hsyn-FLEX-Flpo (titer: 1.00 × 10^{13} vg/ml) and CTB 555 (0.2%, C34776, Thermo
377 Fisher; used solely for determining the injection site) was injected into the spinal cord. In

378 control experiments, rAAV2/9-EF1a-DIO-EYFP (titer: 4.20 × 10^{12} vg/ml) and rAAV2/9-EF1a-
379 DIO-mCherry (titer: 5.28 × 10^{12} vg/ml) were used. All viruses were purchased from Obio
380 Biotechnology Co., Ltd. (Shanghai, China), Taitool Bioscience Co., Ltd. (Shanghai, China), or
381 BrainVTA Co., Ltd. (Wuhan, China).

382 **Stereotaxic injections and optical fiber implant**

383 To target PMC^{ESR1+} neurons, ESR1-Cre mice were anesthetized with isoflurane (3% for
384 induction and 1.5–2% for maintenance) and head-fixed in a stereotaxic frame (RWD Life
385 Science Co., Ltd.; Shenzhen, China). Body temperature was maintained at 36°C throughout
386 the surgery using a heating pad. Local anesthesia (lidocaine, 6 mg/kg, subcutaneous
387 injection) was administered at the incision site before making the incision. A small cranial
388 hole above the PMC was created using a dental drill. Approximately 80 nl of the viral solution
389 was delivered to the injection site at a controlled rate of 20 nl/min, either unilaterally or
390 bilaterally, using a micro-syringe pump connected to a glass pipette. The coordinates for PMC
391 injections were: anteroposterior (AP) is -5.45 mm, mediolateral (ML) is ± 0.70 mm, and
392 dorsoventral (DV) is -3.14 mm from the dura. The pipette was then slowly withdrawn over 5
393 min to prevent virus overflow. The incision was closed with sutures, and the mice received
394 antibiotics and analgesics post-surgery. A heating pad was used for the mice to aid recovery
395 from anesthesia. The mice were then group-housed in their home cages for 3-4 weeks to
396 allow for viral expression.

397 For optic fiber implantation, the optic fiber (NA: 0.48, diameter: 200 µm, Doric lenses,
398 Quebec City, QC, Canada) was fixed into a metal cannula and positioned 50 µm above the
399 PMC injection site. The fiber was implanted unilaterally for photometry experiments and
400 bilaterally for optogenetics experiments. Dental cement was used to affix the optical fiber to
401 the skull. Mice were housed individually and given 3-5 days to recover before recording or
402 stimulation sessions. After the experiments, the placement of the virus and optical fiber was
403 confirmed by histology in each mouse.

404 **Targeted spinal cord injections**

405 For spinal cord injection surgery, the method previously described was used (Chen et al.,
406 2019). Briefly, mice were anesthetized under isoflurane (1.5-2% oxygen) and positioned on a
407 heating pad. After shaving the hair, a midline skin incision (1-2 cm) was performed over the
408 lumbar segments following local anesthesia (lidocaine, 6 mg/kg, subcutaneous injection) at
409 the incision site. The tissue and muscle connected to the dorsal spine were dissected to

410 expose the T12-L2 vertebrae. The spine was affixed to a stereotactic frame using a spinal
411 adapter (68094, RWD), and the spinal cord between L1 and L2 was exposed by removing the
412 ligamentous and epidural membranes. Using the central vein as a reference, a total of 80 nL
413 of virus solution was injected at two different locations, each injection (40 nL) was
414 administered through a micro-syringe pump connected to a glass pipette, targeting DGC (+
415 0.12 mm lateral to the central vein, 0.52 mm deep from the dorsal surface at a 10-degrees
416 angle) and SPNs (- 0.12 mm lateral to the central vein, 0.52 mm deep from the dorsal surface
417 at a 30-degrees angle). The pipette remained in position for a minimum of 5 min before
418 being slowly removed to prevent any leakage. The injection sites were sealed with tissue
419 glue (Vetbond, 3M Animal Care Products), followed by suturing of the skin. Mice received
420 antibiotics and analgesics post-surgery. Approximately 3-4 weeks after the injections, the
421 brain and spinal cords were extracted for histological validation. In ESR1-Cre or CRH-Cre mice,
422 PMC cells projecting to the SPN (labeled with mCherry) and DGC (labeled with EGFP) regions
423 of the spinal cord were manually quantified using Image J.

424 **Pudendal nerve and pelvic nerve transection**

425 Pudendal nerve transection was performed as described previously (Khorramirouz et al.,
426 2016; Peh et al., 2018). Briefly, mice were anesthetized with isoflurane (1.5-2% oxygen) and
427 positioned on a heating pad. A midline skin incision was made along the back from L4 to the
428 coccyx, followed by paraspinal incisions through the gluteal muscles and fascia to expose the
429 sciatic nerve. The sciatic nerve was gently retracted to expose the pudendal nerve. Using
430 microsurgical scissors, the bilateral pudendal nerves, along with the anastomotic branch,
431 were carefully dissected and excised.

432 For pelvic nerve transection, modifications to the established method (Chang et al.,
433 2018) were made to minimize surgical trauma. Mice were positioned laterally, and bilateral
434 paraspinal incisions were extended upward. The sciatic and pudendal nerves were gently
435 retracted laterally to expose the pelvic nerve, which was identified (originating from the
436 sacral segments of the spinal cord and connecting to the major pelvic ganglion) and severed.
437 For pelvic nerve transection experiments in freely moving mice, the muscles and skin were
438 sutured, and antibiotics and analgesics were administered. In the sham injury group, the
439 same procedures were followed, except for the transection of the pelvic nerve.

440 **Fiber photometry recording and analysis in freely behaving mice**

441 The Ca^{2+} recordings of PMC^{ESR1+} neurons were conducted using a fiber photometry setup, as
442 described previously (Yao et al., 2018; Rao et al., 2022). Fluorescence at the fiber tip was

443 excited by blue light (0.22 mW/mm^2). Mice with implanted fibers were injected
444 intraperitoneally with diuretics (furosemide, 40 mg/kg) and acclimated in a testing chamber
445 equipped with a bottom camera (1,280 × 720 pixels) for 20 min before recording. Signals
446 from PMC^{ESR1+} neurons and voiding behavior were simultaneously recorded for
447 approximately 40 min. Ca^{2+} signals were sampled at 2000 Hz using NI LabVIEW software
448 (National Instruments, USA), while behavioral video was captured at 30 Hz. Fiber photometry
449 data and video were synchronized via event markers. For data analysis, all signals were
450 processed with a Savitzky-Golay filter (third-order polynomial, 50 side points) for low-pass
451 filtering. $\Delta f/f = (f - f_{baseline})/f_{baseline}$ was calculated to assess photometry signals during voiding,
452 where $f_{baseline}$ represents the minimum fluorescence recorded. Results were presented as
453 heatmaps using MATLAB. Ca^{2+} signal data were shuffled by dividing the original dataset into
454 10 segments and randomly associating them with voiding events. Positive signals were
455 defined as Ca^{2+} signal amplitudes exceeding three times the noise band (the standard
456 deviation). This procedure was also applied to control mice to correct for movement
457 artifacts.

458 **Single-unit with optrode recording and analysis**

459 To identify the single-unit activity of PMC^{ESR1+} neurons, optrode recordings were performed
460 as described previously (Qin et al., 2022; Qin et al., 2018; Yang et al., 2023). Briefly, the
461 optrode consisted of a 200 µm optical fiber and four tetrode assemblies aligned in a line,
462 spaced 100 µm apart. The optical fiber was secured to the electrodes, positioned 500 µm
463 above their tips, and connected to an LED. Each electrode assembly comprised four twisted
464 tungsten wires (25 µm, California Fine Wire), allowing vertical movement via
465 micromanipulators. Optrode implantation surgery was performed in ESR1-Cre mice
466 expressing ChR2 in the PMC, with the electrode tips aligned and implanted 2.80 mm below
467 the brain dura. After a recovery period of 5-7 days, the tetrodes were slowly inserted to a
468 target depth of -2.95 mm and recording began. Single-unit signals from PMC^{ESR1+} neurons in
469 freely behaving mice were recorded using an RHD2000 USB board (C3100, Intan Technology)
470 at 20 kHz, while behavioral video was captured simultaneously. Units with short spike
471 latencies (< 7 ms) in response to light pulses of varying intensities (5 mW, 10 mW, 15 mW,
472 and 20 mW) and high responsiveness (> 70 %) were identified as PMC^{ESR1+} cells. To confirm
473 recording locations, electro-lesions were performed by applying a current (10 µA, 12 s)
474 through the tetrodes.

The raw recorded data were preprocessed using established methods to extract peaks (Qin et al., 2018). All events exceeding the amplitude threshold (set at four standard deviations above the background) were kept for further analysis. The average firing rate of each cell was calculated within a sliding time bin of 20 seconds around voiding (0.1 s intervals), divided by the total number of trails, and adjusted by subtracting the baseline value (the median firing rate during the -10 to -5 s before voiding). The results were visualized as a heatmap (logarithmic analysis) in Figure 1. Statistical analysis of the average firing rates over a 2-second interval before voiding (from -10 s to -8 s) and around voiding (from -1 s to 1 s) was conducted for PMC^{ESR1+} neurons and non-PMC^{ESR1+} neurons, respectively.

Optogenetic experiments in freely behaving mice

Before optogenetic stimulation, mice underwent the same procedures as for fiber photometry: they received a diuretic with the intraperitoneal injection to increase urination events and were acclimated to the testing chamber for at least 20 min. For optogenetic inhibition experiments, bilateral stimulation (1 mW/mm^2 at fiber tips, 50 Hz frequency, 20 ms pulses) was delivered using 473 nm blue light. To assess the effect of light inhibition on urination, mice were placed in a glass chamber (28 cm × 16 cm × 30 cm) with a 0.19 mm filter paper (14.6 cm × 27 cm, BWD) underneath. Urination was observed at three stages: pre-photoinhibition (light-off), during the 5 s or 60 s of photoinhibition (light-on), and post-photoinhibition (light-off). The photoinhibition parameters (frequency and duration) were controlled via the NI LabVIEW platform (National Instruments, USA). Real-time urination behavior was monitored simultaneously using two cameras positioned above and below the glass chamber (Chongqing NewLight Co., Ltd; see: www.newlightxhr.com). The laser was manually triggered at the onset of urination (within 4 s), and experiments where the trigger exceeded 4 s were excluded. Urination cessation was defined as the initiation of movement after urination. The void area, total void duration, and latency were analyzed from the video and are presented in Figure 2 and Figures supplement 5 and 6.

For optogenetic activation experiments, bilaterally fiber-implanted mice were connected to two 473-nm blue laser generators (5 mW/mm^2 at fiber tips, 25 Hz frequency, 15 ms pulses) via optic fibers. During testing, blue light was delivered for 5 s with approximately 3-min intervals between trials, over a 30-45 min session. This light stimulation was repeated over two days with a one-day interval. Mouse behavior was monitored and recorded simultaneously. The stimulation was performed before and after transection for photoactivation experiments in freely behaving mice with pelvic nerve transection using the

509 same procedures. Note that the photostimulation experiments for pelvic nerve transactions
510 were conducted one day after the surgery. Detailed success rates, latency of voiding, and
511 void area after photoactivation are shown in Figures 3 and 6.

512 **Simultaneous cystometry and electromyography in anesthetized mice**

513 Bladder catheter and urethral sphincter electrode implantation were performed as
514 previously described (Verstegen et al., 2019; Hou et al., 2016; Keller et al., 2018). Briefly,
515 adult fiber-implanted ESR1-Cre mice were anesthetized with isoflurane and placed on a
516 heating pad. A lower mid-abdomen incision exposed the bladder and urethral sphincter. PE-
517 10 tubing was inserted through the bladder dome and secured with a 6-0 Ethicon suture. For
518 electromyography (EMG) recording, two 160 µm silver-plated copper wire electrodes (P/N
519 B34-1000, USA) with 2 mm exposed tips were inserted into the external urethral sphincter
520 (EUS) on both sides using a 30-gauge needle, positioned between the urethra and pubic
521 symphysis, and spaced at least 2 mm apart. A ground wire with 4 mm exposed tips was
522 inserted subcutaneously near the sternal notch to minimize signal interference. The ends of
523 the bladder catheter tubing and wire electrodes were exteriorized through an incision on the
524 skin at the back of the neck, and both abdominal and neck incisions were closed. For
525 measuring intravesical pressure, the bladder tubing was connected to a pressure transducer
526 (YPJ01H; Chengdu Instrument Factory, China) and a syringe pump (RWD404; RWD
527 Technology Corp., Ltd., China) via three-way stopcocks. Bladder pressure and EUS-EMG data
528 were recorded through a multi-channel physiological recording device (RM6240; Chengdu
529 Instrument Factory, China) sampled at 8 kHz. After surgery, mice were permitted to recover
530 from anesthesia and resume walking.

531 For simultaneous recording, all fiber-implanted mice were anesthetized with urethane
532 (1.2 g/kg, i.p.) and continuously infused with room-temperature physiological saline at 30-50
533 µl/min via the bladder catheter for at least 45 min. Recording or stimulation was performed
534 once regular bladder pressure cycles associated with natural urination events were
535 established. “Filling bladder” was defined as continuous saline infusion, while “non-filling
536 bladder” was defined as no infusion. Cystometry and EUS-EMG data were captured via
537 commercial acquisition software, alongside monitoring of Ca^{2+} signals and mouse behavior.
538 For cross-correlation analysis, cystometric data, EMG data, and photometry data were first
539 downsampled to 40 Hz and standardized using z-scored. The original EMG data were
540 processed to extract their envelope using MATLAB’s “envelope” function. The original data
541 were merged, and divided into 10 segments, and segments of photometry data were

542 randomly matched with segments of cystometry or envelope EMG data to create shuffled
543 datasets. Cross-correlations of cystometric and photometry data, or EMG and photometry
544 data were calculated using MATLAB's "xcorr" function, and the peak values of cross-
545 corrections were reported, as shown in Supplementary Figure 3.

546 For photoactivation experiments performed simultaneously with cystometry and
547 electromyography recording, blue light pulses were delivered periodically (every 30 s) at 25
548 Hz for 15 ms, lasting 5 s, or randomly at intervals between 20 s and 40 s, with each condition
549 repeated at least 15 times. For photoactivation experiments performed simultaneously with
550 cystometry and urethral electromyography recording under pelvic or pudendal nerve
551 transection conditions, the surgical procedures and pre-recording preparations were the
552 same as those described above, with the following changes: Mice underwent three stages of
553 randomized photostimulation (consisted of 25 Hz, 15 ms, 5-s durations, with intervals
554 between 30 s and 60 s) in sequence under urethane anesthesia (1.2 g/kg, i.p.): an intact
555 nerve period, a pudendal nerve or pelvic nerve transection period, and a period with both
556 pudendal nerve and pelvic nerve transection. All trials were pooled to assess the impact of
557 nerve transection on bladder and sphincter function for each mouse. Cystometric data,
558 including $\Delta P = P_{5\,sec} - P_{0\,sec}$ (where $P_{0\,sec}$ is the pressure at the onset of laser stimulation and P_5
559 $_{sec}$ is the pressure at the end of laser stimulation) and the pressure ratio $P_{ratio} = P_{max\,(0\text{-}5)sec}$ /
560 $P_{mean\,(-5\text{-}0)sec}$ (where $P_{max\,(0\text{-}5)sec}$ is the maximum pressure from laser onset to cessation, and
561 $P_{mean\,(-5\text{-}0)sec}$ is the average pressure during the 5 seconds preceding laser onset), were
562 calculated using MATLAB. The EUS-EMG data (burst duration and area under the curve) were
563 analyzed using multi-channel physiological recording software. The spectrogram was
564 generated using envelope EMG data around photostimulation in MATLAB, as shown in
565 Figures 4 and 5, and Figure supplement 8. The onset time of bladder pressure upstroke was
566 identified by finding the maximum of the second derivative of cystometry curves around
567 pressure peaks using a MATLAB script. The onset time of EMG bursting (Kadekawa et al.,
568 2016b; Cheng, 2004) was manually defined as the points at which bursting activity begins.
569 The results are shown in Figure 8.

570 For photoinhibition experiments performed simultaneously with cystometry and
571 electromyography recording, the light was manually triggered at the onset of EMG bursts
572 and delivered in 20 ms pulses at 50 Hz for either 5 s or 60 s. Cystometric data, including
573 $\Delta pressure = P_{peak} - P_{min}$ (where P_{peak} is the peak pressure and P_{min} is the minimum pressure
574 after the peak) and threshold pressure (bladder pressure upstroke), were analyzed manually
575 using the multi-channel physiological recording software. The EUS-EMG data (burst duration,

576 area under the curve, and latency of termination) was analyzed using the multi-channel
577 physiological recording software. The latency of bursting termination is defined as the
578 interval from laser onset to the end of EUS-EMG bursting. The end time of bladder pressure
579 upstroke (termination of the rapid increase in bladder pressure before the end of voiding,
580 denoting bladder relaxation) was identified by finding the minimum of the second derivative
581 of cystometry curves around pressure peaks using a MATLAB script. The end time of EMG
582 bursting was manually defined as the points at which the onset of tonic activity after
583 bursting. The results are shown in Figures 3 and 8.

584 **Histology and immunohistochemistry**

585 Following the completion of all experiments, histological verification of fiber implantation or
586 virus injection positions was conducted. Mice were deeply anesthetized with 1% sodium
587 pentobarbital (10 ml/kg), followed by transcardial perfusion with cold 0.9% saline and 4%
588 paraformaldehyde (PFA). The brain or spinal cord (in some experiments) was then extracted
589 and post-fixed overnight at 4 °C in ice-cold 4% PFA. Coronal brain sections (40 μm) and the
590 thoracolumbar and lumbosacral segments of spinal cord sections (70 μm) were cut using a
591 freezing microtome. For TH immunohistochemistry, free-floating sections were initially
592 incubated in 1% PBST (1% Triton X-100 in PBS, Sigma) for 60 min. The sections were blocked
593 with 10% donkey serum (Sigma) in 0.1% PBST for 2 hours at room temperature. Following
594 blocking, then incubated at 4°C for 24 hours with anti-TH antibodies (1:200 dilution, rabbit,
595 Sigma-Aldrich). After extensive washing with PBS, sections were incubated with a secondary
596 antibody (1:300, Alexa Fluor 488 or 594 donkey anti-rabbit, Invitrogen) at room temperature
597 for 2 hours. Finally, all sections, including the target segments of the spinal cord, were
598 incubated with DAPI (1:1000, Beyotime) for 15 min. Images were acquired using a confocal
599 microscope (TCS SP5, Leica) equipped with × 4, × 10, and × 20 oil objectives, utilizing 405 nm,
600 488 nm, and 552 nm lasers, or with an Olympus microscope.

601 **Statistical analysis**

602 All data were processed and statistically analyzed using Prism 8 GraphPad, MATLAB, and SPSS
603 22 software. For unpaired group comparisons, the Wilcoxon rank-sum test was used, and for
604 paired groups, the Wilcoxon signed-rank test was applied, as described in the figure legends.
605 Analysis was performed by investigators blinded to the experiments. The n value reflects the
606 final number of animals in each experiment group, with animals excluded if histological
607 verification of gene expression showed poor or absent. Data are represented as median with

25%-75% percentiles, and statistical significance was defined as * < 0.05, ** < 0.01, *** < 0.001; ns, no significant difference.

Acknowledgments

The authors are grateful to Ms. Jia Lou for her help in composing and editing the layout of the figures. This study was supported by grants from the National Natural Science Foundation of China to X.C. (No. 31925018, 32127801), the National Key R&D Program of China to X.C. (2021YFA0805000), the Suzhou Science and Technology Plan Project (SZS2022008), and the Jiangsu Provincial Big Science Facility Initiative (BM2022010), and the Guangxi Talent Program ("Highland of Innovation Talents"). X.C. is a member of CAS Center for Excellence in Brain Science and Intelligence Technology.

620 ## Additional information

621 **Funding**

Funder	Grant reference number	Author
National Key R&D Program of China	2021YFA0805000	Xiaowei Chen
National Natural Science Foundation of China	31925018	Xiaowei Chen
National Natural Science Foundation of China	32127801	Xiaowei Chen
Suzhou Science and Technology Plan Project	SZS2022008	Hongbo Jia
Jiangsu Provincial Big Science Facility Initiative	BM2022010	Hongbo Jia
Guangxi Talent Program	Highland of Innovation Talents	Hongbo Jia

622

623 **Author contributions**

624 Project design, J.W.Y, and X.C.; injection and histology, X.L., X.P.L., J.L.(1), L.X.Y., and J.L.(2);
625 behavior experiments, X.L., C.H.Y., and X.W.; nerves transection, X.L.; fiber recording, X.L.
626 C.H.Y., and X.P.L.; electrophysiology, X.L., H.Q., T.L.J., and X.W.; fiber recording, X.L. and L.X.Y.;
627 cystometry and electromyography experiments, X.L., X.P.L., and J.L.(1); data interpretation
628 and analysis, X.L., H.Q., S.S.L., H.B.J., X.Liao, J.W.Y., and X.C.; figure preparation, X.L., H.B.J.,
629 J.W.Y, and X.C.; manuscript writing, X.L., H.B.J., J.W.Y, and X.C. with the help of all co-authors.
630 All authors read and commented on the manuscript.

631 **Author ORCIDs**

632 Jiwei Yao: https://orcid.org/0009-0003-5063-6584

633 Xiaowei Chen: https://orcid.org/0000-0003-0906-6666

634 Hongbo Jia: https://orcid.org/0000-0003-1585-2161

635 **Ethics**

636 All experiment procedures were approved by the Third Military Medical University Animal
637 Care and Use Committee (Approval number: AMUWEC20230061) and were conducted
638 strictly in adherence to established guidelines.

639

Additional files

Data availability

Any additional information underlying the findings of this study is available from the corresponding authors upon reasonable request. The supporting data underlying Figures 1-8 and Figures supplement 1-9 are provided as Source Data files. Source Data are provided in this paper.

Code availability

The codes supporting the current study have not been deposited in a public repository, but are available from the corresponding author upon request.

References

Abud EM, Ichiyama RM, Havton LA, Chang HH. 2015. Spinal stimulation of the upper lumbar spinal cord modulates urethral sphincter activity in rats after spinal cord injury. *Am J Physiol Renal Physiol* **308**: F1032-40. DOI: 10.1152/ajprenal.00573.2014.

Andersson, K.-E. 2004. Urinary Bladder Contraction and Relaxation: Physiology and Pathophysiology. *Physiol Reviews* **84**: 935-986. DOI: 10.1152/physrev.00038.2003.

Aoki Y, Brown HW, Brubaker L, Cornu JN, Daly JO, Cartwright R. 2017. Urinary incontinence in women. *Nature Reviews Disease Primers* **3**. DOI: 10.1038/nrdp.2017.42.

Baram TZ, Ressler K, Gunn BG, Molet J, Chen Y. 2015. Diversity of Reporter Expression Patterns in Transgenic Mouse Lines Targeting Corticotropin-Releasing Hormone-Expressing Neurons. *Endocrinology* **156**: 4769-4780. DOI: 10.1210/en.2015-1673.

Benarroch EE. 2010. Neural control of the bladder Recent advances and neurologic implications. *Neurology* **75**: 1839-1846. DOI: 10.1212/WNL.0b013e3181fdabba.

Biallosterski BT, van Koeveringe GA, van Kerrebroeck PE, Gillespie JI, de Wachter SG. 2011. Nonvoiding Activity of the Guinea Pig Bladder. *Journal of Urology* **186**: 721-727. DOI: 10.1016/j.juro.2011.03.123.

Chang H, Yeh J, Ichiyama R, Rodriguez L, Havton L. 2018. Mapping and neuromodulation of lower urinary tract function using spinal cord stimulation in female rats. *Exp Neurol* **305**: 26-32. DOI: 10.1016/j.expneurol.2018.03.007.

Chang HY, Cheng CL, Chen JJJ, de Groat WC. 2007. Serotonergic drugs and spinal cord

670 transections indicate that different spinal circuits are involved in external urethral
671 sphincter activity in rats. *American Journal of Physiology-Renal Physiology* **292**: F1044-
672 F1053. DOI: 10.1152/ajprenal.00175.2006.
673 Chen KS, McGinley LM, Kashlan ON, Hayes JM, Bruno ES, Chang JS, Mendelson FE, Tabbey
674 MA, Johe K, Sakowski SA, Feldman EL. 2019. Targeted intraspinal injections to assess
675 therapies in rodent models of neurological disorders. *Nat Protoc* **14**: 331-349. DOI:
676 10.1038/s41596-018-0095-5.
677 Cheng C. 2004. The role of capsaicin-sensitive afferent fibers in the lower urinary tract
678 dysfunction induced by chronic spinal cord injury in rats. *Experimental Neurology* **187**:
679 445-454. DOI: 10.1016/j.expneurol.2004.02.014.
680 Cho H, Kang T, Chang J, Choi Y, Park M, Choi K, Sung S, Park K, Jung D. 2015. Neuroanatomical
681 correlation of urinary retention in lateral medullary infarction. *Annals of Neurology* **77**:
682 726-733. DOI: 10.1002/ana.24379.
683 de Groat WC. 2009. Integrative control of the lower urinary tract: preclinical perspective.
684 *British Journal of Pharmacology* **147**. DOI: 10.1038/sj.bjp.0706604.
685 de Groat WC, Griffiths D, Yoshimura N. 2015. Neural Control of the Lower Urinary Tract.
686 *Compr Physiol.* **5**: 327-396. DOI: 10.1002/cphy.c130056.
687 Desjardins C, Maruniak J, Bronson F. 1973. Social Rank in House Mice: Differentiation
688 Revealed by Ultraviolet Visualization of Urinary Marking Patterns. *Science* **182**: 939-941.
689 DOI: 10.1126/science.182.4115.939.
690 Drake MJ, Williams J, Bijos DA. 2014. Voiding dysfunction due to detrusor underactivity: an
691 overview. *Nature Reviews Urology* **11**: 454-464. DOI: 10.1038/nrurol.2014.156.
692 Fang YY, Yamaguchi T, Song SC, Tritsch NX, Lin D. 2018. A Hypothalamic Midbrain Pathway
693 Essential for Driving Maternal Behaviors. *Neuron* **98**: 192-207.e10. DOI:
694 10.1016/j.neuron.2018.02.019.
695 Fowler C, Griffiths D, de Groat W. 2008. The neural control of micturition. *Nat Rev Neurosci.*
696 **9**: 453-466. DOI: 10.1038/nrn2401.
697 Griffiths D. 2015. Neural control of micturition in humans: a working model. *Nature Reviews*
698 *Urology* **12**: 695-705. DOI: 10.1038/nrurol.2015.266.
699 Griffiths D, Derbyshire S, Stenger A, N. R. 2005. Brain control of normal and overactive
700 bladder. *J Urol* **174**: 1862-1867. DOI: 10.1097/01.ju.0000177450.34451.97.
701 Hou XH, Hyun M, Taranda J, Huang KW, Todd E, Feng D, Atwater E, Croney D, Zeidel ML,
702 Osten P, Sabatini BL. 2016. Central Control Circuit for Context-Dependent Micturition. *Cell*
703 **167**: 73-86 e12. DOI: 10.1016/j.cell.2016.08.073.

704 Hyun M, Taranda J, Radeljic G, Miner L, Wang W, Ochandarena N, Huang KW, Osten P,
705 Sabatini B. 2021. Social isolation uncovers a brain-wide circuit underlying context-
706 dependent territory-covering micturition behavior. *Proc Natl Acad Sci U S A.* **118**:
707 e2018078118. DOI: 10.1101/798132.
708 Ito H, Sales AC, Fry CH, Kanai AJ, Drake MJ, Pickering AE. 2020. Probabilistic, spinally-gated
709 control of bladder pressure and autonomous micturition by Barrington's nucleus CRH
710 neurons. *eLife* **9**: e56605. DOI: 10.7554/eLife.56605.
711 Jin WK, Su JK, Jong MP, Yong GN, Khae HK. 2020. Past, Present, and Future in the Study of
712 Neural Control of the Lower Urinary Tract. *24*: 191-199. DOI: 10.5213/inj.2040318.159.
713 Kadekawa K, Yoshimura N, Majima T, Wada N, Shimizu T, Birder LA, Kanai AJ, de Groat WC,
714 Sugaya K, Yoshiyama M. 2016a. Characterization of bladder and external urethral activity
715 in mice with or without spinal cord injury--a comparison study with rats. *Am J Physiol*
716 *Regul Integr Comp Physiol* **310**: R752-8. DOI: 10.1152/ajpregu.00450.2015.
717 Kadekawa K, Yoshimura N, Majima T, Wada N, Shimizu T, Birder LA, Kanai AJ, de Groat WC,
718 Sugaya K, Yoshiyama M. 2016b. Characterization of bladder and external urethral activity
719 in mice with or without spinal cord injury—a comparison study with rats. *American*
720 *Journal of Physiology-Regulatory, Integrative and Comparative Physiology* **310**: R752-R758.
721 DOI: 10.1152/ajpregu.00450.2015.
722 Karigo T, Kennedy A, Yang B, Liu M, Tai D, Wahle I, Anderson D. 2021. Distinct hypothalamic
723 control of same- and opposite-sex mounting behaviour in mice. *Nature* **589**: 258-263. DOI:
724 10.1038/s41586-020-2995-0.
725 Kaur Angeldeep W, Ackels T, Kuo T-H, Cichy A, Dey S, Hays C, Kateri M, Logan Darren W,
726 Marton Tobias F, Spehr M, Stowers L. 2014. Murine Pheromone Proteins Constitute a
727 Context-Dependent Combinatorial Code Governing Multiple Social Behaviors. *Cell* **157**:
728 676-688. DOI: 10.1016/j.cell.2014.02.025.
729 Kawatani M, de Groat WC, Itoi K, Uchida K, Sakimura K, Yamanaka A, Yamashita T, Kawatani
730 M. 2021. Downstream projection of Barrington's nucleus to the spinal cord in mice. *126*.
731 DOI: 10.1152/jn.00026.2021.
732 Keller JA, Chen J, Simpson S, Wang EH-J, Lilascharoen V, George O, Lim BK, Stowers L. 2018.
733 Voluntary urination control by brainstem neurons that relax the urethral sphincter. *Nature*
734 *Neuroscience* **21**: 1229-1238. DOI: 10.1038/s41593-018-0204-3.
735 Khorramirouz R, Mozafarpour S, Kameli SM, Ladi Seyedian SS, Oveisi N, Rahimi Z, Alijani M,
736 Kajbafzadeh AM. 2016. A Novel Method of Urinary Sphincter Deficiency: Serial
737 Histopathology Evaluation in a Rat Model of Urinary Incontinence. *Anat Rec (Hoboken)*

299: 173-80. DOI: 10.1002/ar.23291.

Langdale CL, Grill WM. 2016. Phasic activation of the external urethral sphincter increases voiding efficiency in the rat and the cat. *Experimental Neurology* **285**: 173-181. DOI: 10.1016/j.expneurol.2016.05.030.

Lee C, Lee J, Park J, Na H, Shin J, Na Y, Kim K. 2021. Sophisticated regulation of micturition: review of basic neurourology. *J Exerc Rehabil* **17**: 295-307. DOI: 10.12965/jer.2142594.297.

Lee H, Kim D, Remedios R, Anthony T, Chang A, Madisen L, Zeng H, Anderson D. 2014. Scalable control of mounting and attack by Esr1+ neurons in the ventromedial hypothalamus. *Nature* **509**: 627-632. DOI: 10.1038/nature13169.

Liu M, Kim D, Zeng H, Anderson D. 2022. Make war not love: The neural substrate underlying a state-dependent switch in female social behavior. *Neuron.* **110**: 841-856. DOI: 10.1016/j.neuron.2021.12.002.

Mallory B. 1991. Pharmacological modulation of the pontine micturition center. *Brain Research* **546**: 310-320. DOI: 10.1016/0006-8993(91)91495-m.

Malykhina AP. 2017. How the brain controls urination. *eLife* **6**. DOI: 10.7554/eLife.33219.

Manohar A, Curtis AL, Zderic SA, Valentino RJ. 2017. Brainstem network dynamics underlying the encoding of bladder information. *Elife* **6**. DOI: 10.7554/eLife.29917.

Milsom I, Coyne KS, Nicholson S, Kvasz M, Chen C-I, Wein AJ. 2014. Global Prevalence and Economic Burden of Urgency Urinary Incontinence: A Systematic Review. *European Urology* **65**: 79-95. DOI: 10.1016/j.eururo.2013.08.031.

Morrison JFB. 2008. The discovery of the pontine micturition centre by F. J. F. Barrington. *Experimental Physiology* **93**: 742-745. DOI: 10.1113/expphysiol.2007.038976.

Mukhopadhyay S, Stowers L. 2020. Choosing to urinate. Circuits and mechanisms underlying voluntary urination. *Current Opinion in Neurobiology* **60**: 129-135. DOI: 10.1016/j.conb.2019.11.004.

Noto H, Roppolo J, Steers W, de Groat W. 1989. Excitatory and inhibitory influences on bladder activity elicited by electrical stimulation in the pontine micturition center in the rat. *Brain Research* **492**: 99-115. DOI: 10.1016/0006-8993(89)90893-7.

Peh WYX, Mogan R, Thow XY, Chua SM, Rusly A, Thakor NV, Yen SC. 2018. Novel Neurostimulation of Autonomic Pelvic Nerves Overcomes Bladder-Sphincter Dyssynergia. *Front Neurosci* **12**: 186. DOI: 10.3389/fnins.2018.00186.

Qin H, Fu L, Hu B, Liao X, Lu J, He W, Liang S, Zhang K, Li R, Yao J, Yan J, Chen H, Jia H, Zott B, Konnerth A, Chen X. 2018. A Visual-Cue-Dependent Memory Circuit for Place Navigation. *Neuron* **99**: 47-55 e4. DOI: 10.1016/j.neuron.2018.05.021.

Qin H, Fu L, Jian T, Jin W, Liang M, Li J, Chen Q, Yang X, Du H, Liao X, Zhang K, Wang R, Liang S, Yao J, Hu B, Ren S, Zhang C, Wang Y, Hu Z, Jia H, Konnerth A, Chen X. 2022. REM sleep-active hypothalamic neurons may contribute to hippocampal social-memory consolidation. *Neuron* **110**: 4000-4014 e6. DOI: 10.1016/j.neuron.2022.09.004.

Rana S, Alom F, Martinez RC, Fuller DD, Mickle AD. 2024. Acute ampakines increase voiding function and coordination in a rat model of SCI. *Elife* **12**. DOI: 10.7554/eLife.89767.

Rao Y, Gao Z, Li X, Li X, Li J, Liang S, Li D, Zhai J, Yan J, Yao J, Chen X. 2022. Ventrolateral Periaqueductal Gray Neurons Are Active During Urination. *Frontiers in Cellular Neuroscience* **16**. DOI: 10.3389/fncel.2022.865186.

Sakakibara, Ryuji. 2015. Lower urinary tract dysfunction in patients with brain lesions. *Neurology of Sexual and Bladder Disorders* **130**: 269-287. DOI: 10.1016/b978-0-444-63247-0.00015-8.

Sartori AM, Hofer AS, Scheuber MI, Rust R, Kessler TM, Schwab ME. 2022. Slow development of bladder malfunction parallels spinal cord fiber sprouting and interneurons' loss after spinal cord transection. *Exp Neurol* **348**: 113937. DOI: 10.1016/j.expneurol.2021.113937.

Seseke S, Leitsmann C, Hijazi S, Trojan L, Dechent P. 2019. Functional MRI in patients with detrusor sphincter dyssynergia: Is the neural circuit affected? *Neurourology and Urodynamics* **38**: 2104-2111. DOI: 10.1002/nau.24112.

Stoffel J. 2016. Detrusor sphincter dyssynergia: a review of physiology, diagnosis, and treatment strategies. *Transl Androl Urol.* **5**: 127-135. DOI: 10.3978/j.issn.2223-4683.2016.01.08.

Sugaya K, De Groat W. 1994. Micturition reflexes in the in vitro neonatal rat brain stem-spinal cord-bladder preparation. *Am J Physiol.* **266**: R658-67. DOI: 10.1152/ajpregu.1994.266.3.r658.

Taweel, Al, Waleed, Seyam, Raouf. 2015. Neurogenic bladder in spinal cord injury patients. *Research and Reports in Urology*. DOI: 10.2147/rru.S29644.

Valentino RJ, Wood SK, Wein AJ, Zderic SA. 2010. The bladder–brain connection: putative role of corticotropin-releasing factor. *Nature Reviews Urology* **8**: 19-28. DOI: 10.1038/nrurol.2010.203.

Van Batavia JP, Butler S, Lewis E, Fesi J, Canning DA, Vicini S, Valentino RJ, Zderic SA. 2021. Corticotropin-Releasing Hormone from the Pontine Micturition Center Plays an Inhibitory Role in Micturition. *The Journal of Neuroscience* **41**: 7314-7325. DOI: 10.1523/jneurosci.0684-21.2021.

Vanderhorst VGJM, Gustafsson JÅ, Ulfhake B. 2005. Estrogen receptor-α and -β

immunoreactive neurons in the brainstem and spinal cord of male and female mice: Relationships to monoaminergic, cholinergic, and spinal projection systems. *Journal of Comparative Neurology* **488**: 152-179. DOI: 10.1002/cne.20569.

Verstegen A, Vanderhorst V, Gray P, Zeidel M, Geerling J. 2017. Barrington's nucleus: Neuroanatomic landscape of the mouse "pontine micturition center". *J Comp Neurol* **525**: 2287-2309. DOI: 10.1002/cne.24215.

Verstegen AMJ, Klymko N, Zhu L, Mathai JC, Kobayashi R, Venner A, Ross RA, VanderHorst VG, Arrigoni E, Geerling JC, Zeidel ML. 2019. Non-Crh Glutamatergic Neurons in Barrington's Nucleus Control Micturition via Glutamatergic Afferents from the Midbrain and Hypothalamus. *Current Biology* **29**: 2775-2789.e7. DOI: 10.1016/j.cub.2019.07.009.

Vincent S, Satoh K. 1984. Corticotropin-releasing factor (CRF) immunoreactivity in the dorsolateral pontine tegmentum: further studies on the micturition reflex system. *Brain Res.* **308**: 387-391. DOI: 10.1016/0006-8993(84)91085-0.

Wood SK, Baez MA, Bhatnagar S, Valentino RJ. 2009. Social stress-induced bladder dysfunction: potential role of corticotropin-releasing factor. *American Journal of Physiology-Regulatory, Integrative and Comparative Physiology* **296**: R1671-R1678. DOI: 10.1152/ajpregu.91013.2008.

Xiao W, Jiao ZL, Senol E, Yao J, Zhao M, Zhao ZD, Chen X, Cao P, Fu Y, Gao Z, Shen WL, Xu XH. 2021. Neural circuit control of innate behaviors. *Science China Life Sciences* **65**: 466-499. DOI: 10.1007/s11427-021-2043-2.

Yang X, Chen Q, Jian T, Du H, Jin W, Liang M, Wang R, Chen X, Liao X, Qin H. 2023. Optrode recording of an entorhinal-cortical circuit in freely moving mice. *Biomed Opt Express* **14**: 1911-1922. DOI: 10.1364/BOE.487191.

Yao J, Zhang Q, Liao X, Li Q, Liang S, Li X, Zhang Y, Li X, Wang H, Qin H, Wang M, Li J, Zhang J, He W, Zhang W, Li T, Xu F, Gong H, Jia H, Xu X, Yan J, Chen X. 2018. A corticopontine circuit for initiation of urination. *Nature Neuroscience* **21**: 1541-1550. DOI: 10.1038/s41593-018-0256-4.

Zare A, Jahanshahi A, Rahnama'i M, Schipper S, van Koeveringe G. 2019. The Role of the Periaqueductal Gray Matter in Lower Urinary Tract Function. *Mol Neurobiol* **56**: 920-934. DOI: 10.1007/s12035-018-1131-8.

Zderic SA. 2019. Neuroscience: A New Golden Age for Neurourology. *Current Biology* **29**: R880-R883. DOI: 10.1016/j.cub.2019.08.009.

Figures

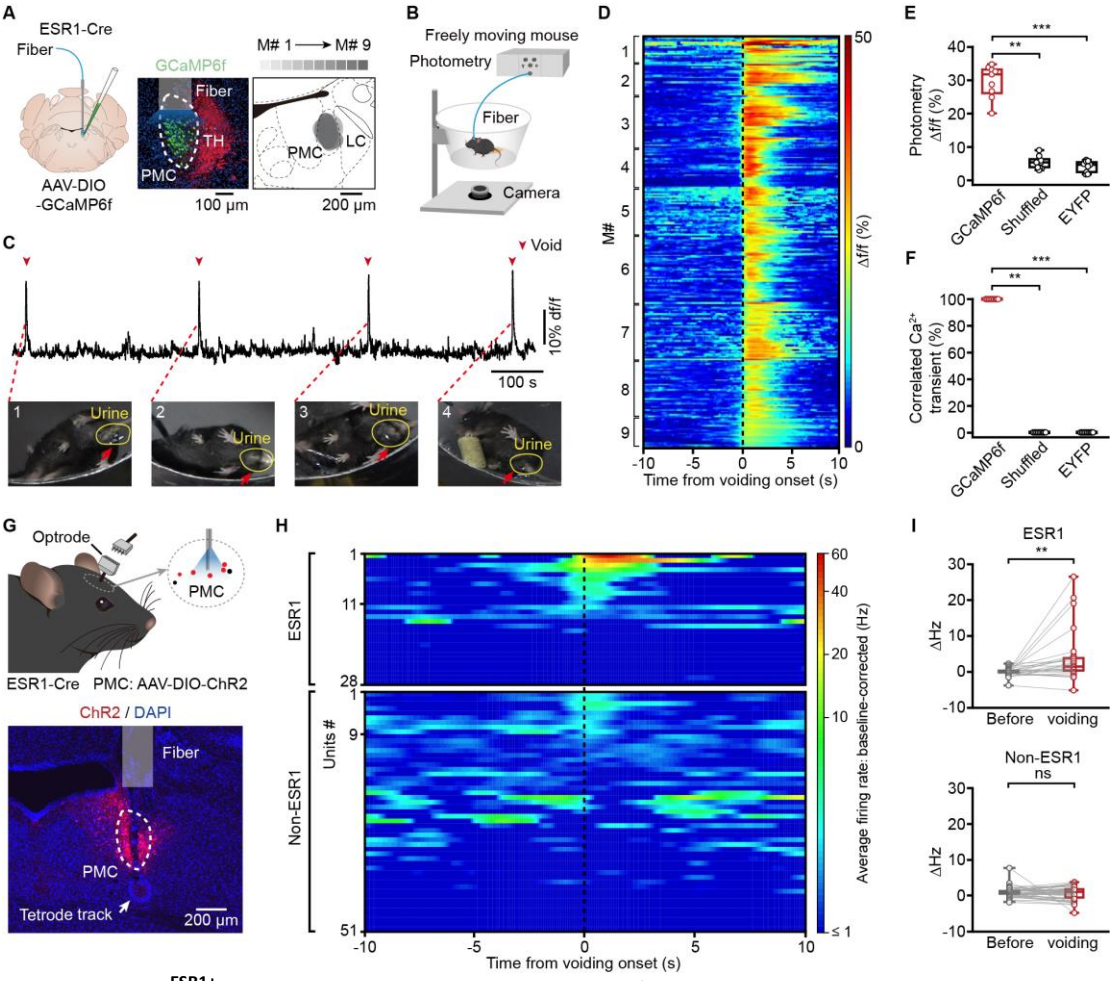

Figure 1. PMC^{ESR1+} cells tightly correlate with successful voiding.

(**A**) Schematic (left) of labeling and representative histology (middle) of PMC^{ESR1+} cells labeled with GCaMP6f. Scale bar: 100 µm. TH (tyrosine hydroxylase) stained neurons in the locus coeruleus. Right: Overlay of GCaMP6f-labelled areas from 9 mice. Scale bar: 200 µm. (**B**) Schematic of fiber photometry Ca^{2+} recording in a freely moving mouse. (**C**) Representative Ca^{2+} traces (top) and voiding events (bottom, yellow circle). (**D**) Cumulative sessions of Ca^{2+} signals aligned to voiding onset (dotted line). (**E**) Boxplots showing the amplitude of voiding-related Ca^{2+} signals in various groups (n = 9 mice per group, 31.8%\26.7%-33.2% for Gcamp6f, 5.4%\3.7%-6.0% for Shuffled, 4.7%\2.5%-5.7% for EYFP, $^{**}P$ = 3.9e-3 (Gcamp6f versus Shuffled), Wilcoxon signed-rank test; $^{***}P$ = 4.1e-5 (Gcamp6f versus EYFP), Wilcoxon rank-sum test). (**F**) Detected voiding-related Ca^{2+} events in various groups (n = 9 mice per group, 100%\100%-100% for Gcamp6f, 0%\0%-0% for Shuffled, 0%\0%-0% for EYFP. $^{**}P$ = 3.9e-3 (Gcamp6f versus Shuffled), Wilcoxon signed-rank test; $^{***}P$ = 4.1e-5 (Gcamp6f versus EYFP), Wilcoxon rank-sum test). (**G**) Schematic (top) and representative histology (bottom) of optrode recording in the PMC of an ESR1-cre mouse. Scale bar: 200 µm. (**H**) Cumulative

856 sessions of sorted single-unit activity of PMC^{ESR1+} (upper; n = 28 cells from 4 mice) and non-
857 PMC^{ESR1+} cells (lower; n = 51 cells from 4 mice) aligned to voiding onset (black dashed line),
858 vertically arranged by their instantaneous firing rate at the voiding onset. (**I**) Boxplots
859 showing the baseline-corrected average firing rates before and during voiding among
860 PMC^{ESR1+} (top, n = 28 cells from 4 mice, $^{**}P = 0.004$) and non-PMC^{ESR1+} cells (bottom, n = 51
861 cells from 4 mice, $P = 0.6$; n.s., not significant; Wilcoxon signed-rank test). For all data points
862 in (**E**, **F**), and (**I**), whisker-box plots indicate the median with the 25%-75% percentile as the
863 box, and whiskers represent the minimum and maximum values.
864

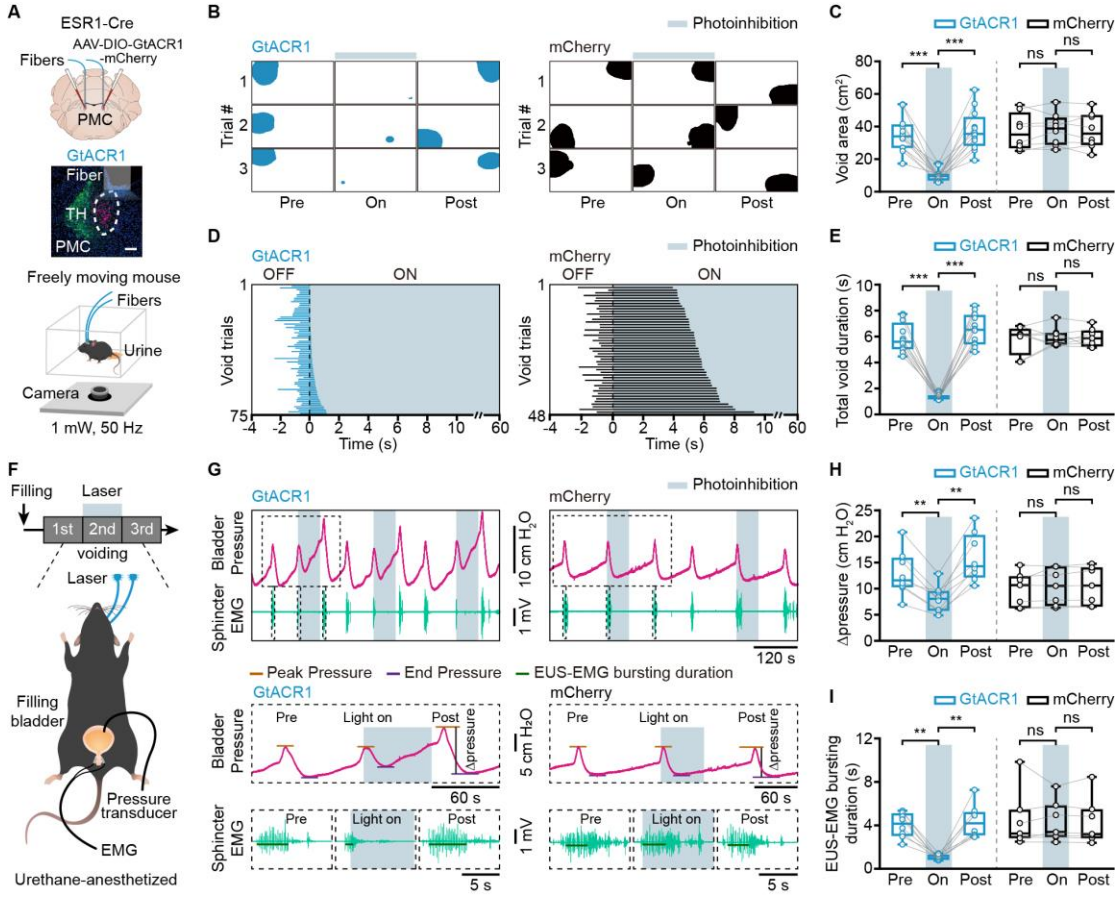

Figure 2. Inactivation of PMC^{ESR1+} cells suppresses bladder contraction and sphincter relaxation to suspend voiding.

(**A**) Schematic of labeling (top), representative histology (middle), and behavior test (bottom) for PMC^{ESR1+} photoinhibition. Scale bar: 100 µm. (**B**, **C**) Representative images (**B**) and quantification (**C**) of the void area before ('Pre'), during ('On'), and after ('Post') photoinhibition in PMC$^{ESR1\text{-}GtACR1}$ (n = 12 mice) and PMC$^{ESR1\text{-}mCherry}$ (n = 8 mice) groups (from left to right: ***P = 4.9e-4, ***P = 4.9e-4, P = 0.3, P = 0.5, respectively; n.s., not significant; Wilcoxon signed-rank test). (**D**) Cumulative trials of voiding duration in PMC$^{ESR1\text{-}GtACR1}$ (blue bar, n = 75 trials from 12 mice) and PMC$^{ESR1\text{-}mCherry}$ (black bar, n = 48 trials from 8 mice) during photoinhibition. Voiding trials are ordered by the increasing time of the voiding epoch with the laser on. (**E**) Voiding duration before, during, and after photoinhibition in PMC$^{ESR1\text{-}GtACR1}$ and PMC$^{ESR1\text{-}mCherry}$ groups (from left to right: ***P = 4.9e-4, ***P = 4.9e-4, P = 0.7, P = 0.9, respectively; n.s., not significant; Wilcoxon signed-rank test). (**F**) Timeline (top) and schematic (bottom) for PMC^{ESR1+} photoinhibition during simultaneous cystometry and electromyography recording. (**G**) Representative traces (top) and expanded portions (bottom) of bladder pressure (magenta) and EUS-EMG (teal) before, during, and after photoinhibition in PMC$^{ESR1\text{-}GtACR1}$ (left) and PMC$^{ESR1\text{-}mCherry}$ (right) groups. (**H**, **I**) Quantification

883 of the Δpressure (**H**) and EUS-EMG bursting duration (**I**) during voiding before, during, and
884 after photoinhibition in $PMC^{ESR1\text{-}GtACR1}$ (n = 8 mice) and $PMC^{ESR1\text{-}mCherry}$ (n = 7 mice) groups (**H:**
885 from left to right: $^{**}P$ = 7.8e-3, $^{**}P$ = 7.8e-3, P = 0.2, P = 0.3, respectively; **I:** from left to
886 right: $^{**}P$ = 7.8e-3, $^{**}P$ = 7.8e-3, P = 0.8, P = 0.4, respectively; n.s., not significant; Wilcoxon
887 signed-rank test). For all data points in (**C**, **E**, **H**), and (**I**), whisker-box plots indicate the
888 median with the 25%-75% percentile as the box, and whiskers represent the minimum and
889 maximum values.

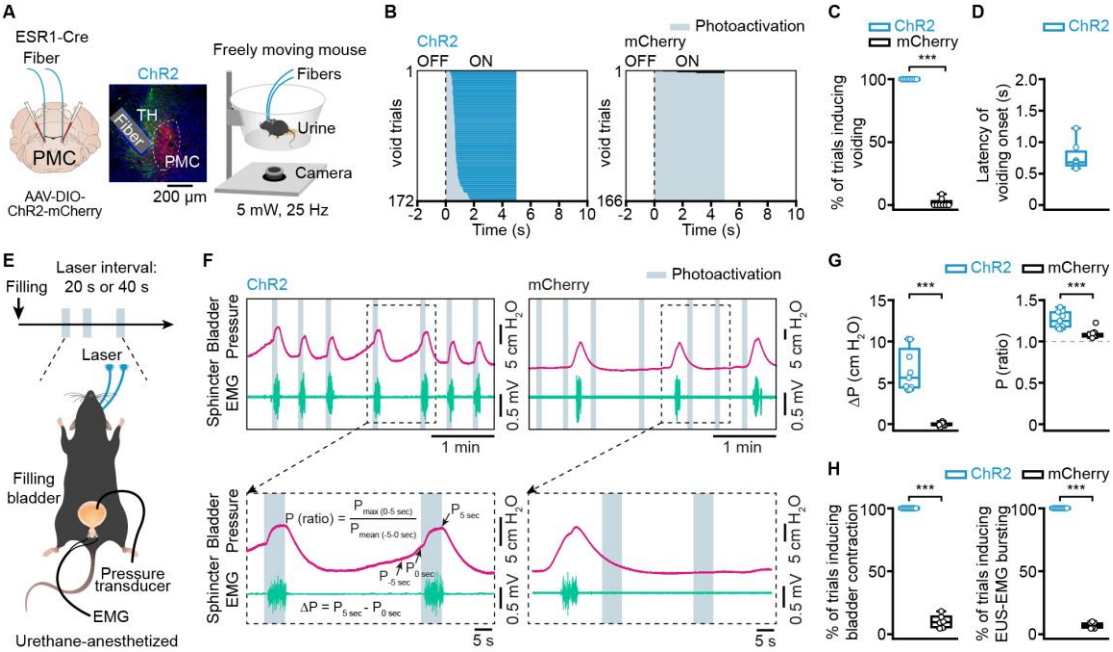

Figure 3. Activation of PMC^{ESR1+} cells induces both bladder contraction and sphincter relaxation to initiate voiding

(**A**) Schematics of labeling (left), representative histology (middle), and behavior test (right) for PMC^{ESR1+} photoactivation. Scale bar: 200 µm. (**B**) Cumulative trials of voiding duration in PMC$^{ESR1\text{-}ChR2}$ (blue bar, n = 172 trials from 8 mice) and PMC$^{ESR1\text{-}mCherry}$ (black bar, n = 166 trials from 8 mice) photoactivation. Voiding trials are ordered by the latency of the voiding epoch with the laser on. (**C**) % of photoactivation-associated voiding events in PMC$^{ESR1\text{-}ChR2}$ and PMC$^{ESR1\text{-}mCherry}$ groups (n = 8 mice per group, ***P = 1.6e-4, Wilcoxon rank-sum test). (**D**) Latency of voiding onset after light on. (**E**) Timeline (top) and schematics (bottom) for PMC^{ESR1+} photoactivation during simultaneous cystometry and electromyography recording. (**F**) Representative traces (top) and expanded portions (bottom) of bladder pressure (magenta) and EUS-EMG (teal) around photoactivation timepoint in PMC$^{ESR1\text{-}ChR2}$ (left) or PMC$^{ESR1\text{-}mCherry}$ (right) groups. (**G**, **H**) Quantification of bladder pressure change (ΔP, **G**, left), the ratio of bladder pressure (**G**, right), the percentage of photoactivation-associated bladder contraction (**H**, left), and the percentage of photoactivation-associated EUS-EMG bursting (**H**, right) upon photoactivation (n = 9 PMC$^{ESR1\text{-}ChR2}$ mice, n = 6 PMC$^{ESR1\text{-}mCherry}$ mice, ***P = 4e-4 for (**G**, **H**), Wilcoxon rank-sum test). For all data points in (**C**, **D**, **G**), and (**H**), whisker-box plots indicate the median with the 25%-75% percentile as the box, and whiskers represent the minimum and maximum values.

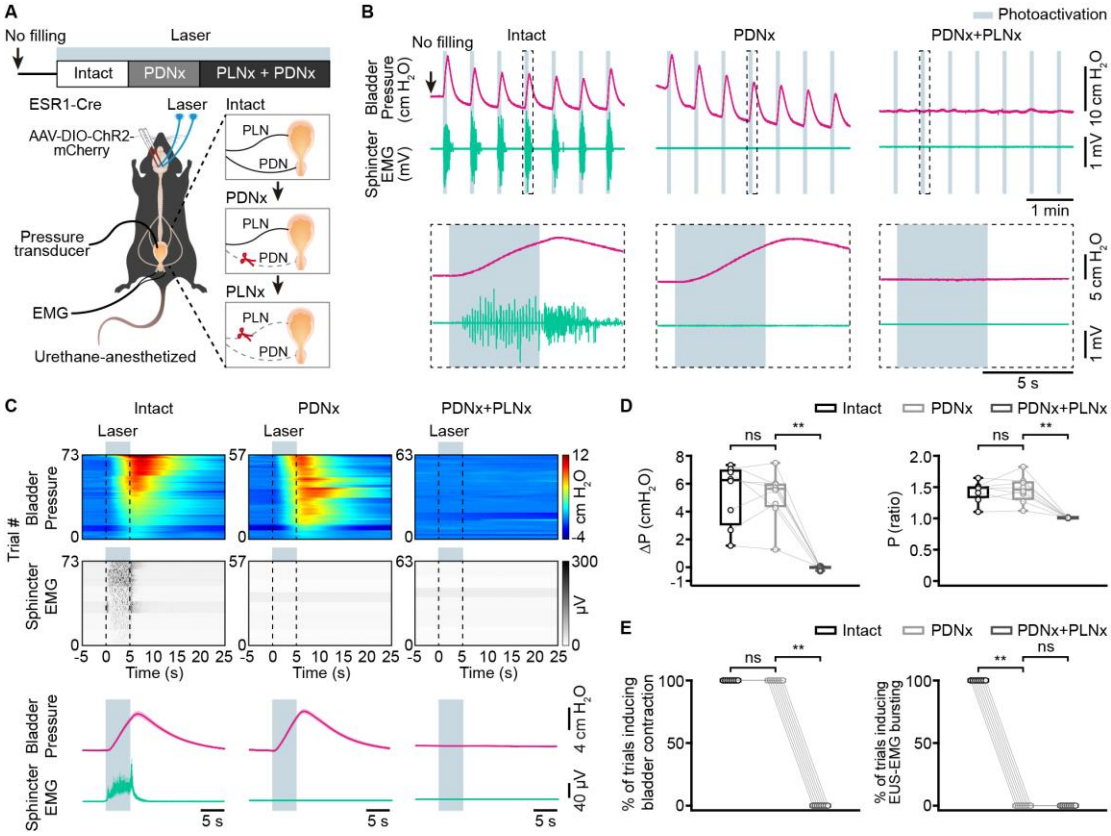

Figure 4. Transection of the pudendal nerves does not impair bladder contraction induced by PMC^{ESR1+} cell photoactivation.

(**A**) Timeline (top) and schematic (bottom) for PMC$^{ESR1\text{-}ChR2}$ photoactivation during simultaneous cystometry and urethral electromyography recordings, with PDNx performed first. PDNx, pudendal nerve transection; PLNx, pelvic nerve transection. (**B**) Representative traces (top) and expanded portions (bottom, from the dashed box in the top panel) showing bladder pressure (magenta) and EUS-EMG (teal) during PMC$^{ESR1\text{-}ChR2}$ photoactivation in various groups, with PDNx performed first. (**C**) Heatmap (top) and average traces (bottom; thick lines and shading represent mean ± s.e.m.) of sorted bladder pressure and EUS-EMG around the photoactivation timepoint for all unfilled bladder trials with the PDNx-first experiment (n = 8 mice per group). (**D, E**) Quantification of bladder pressure change (ΔP, **D**, left), bladder pressure ratio (**D**, right), the percentage of photoactivation-associated bladder contraction (**E**, left), and the percentage of photoactivation-associated EUS-EMG bursting (**E**, right) upon photoactivation for the PDNx-first experiment from (**C**) (n = 8 mice per group, from left to right, **D**: P = 0.8, $^{**}P$ = 7.8e-3, P =0.7, $^{**}P$ = 7.8e-3, respectively; **E**: P = 1, $^{**}P$ = 7.8e-3, $^{**}P$ = 7.8e-3, P = 1, respectively; n.s., not significant; Wilcoxon signed-rank test). For all data points in (**D, E**), whisker-box plots indicate the median with the 25%-75% percentile as the box, and whiskers represent the minimum and maximum values.

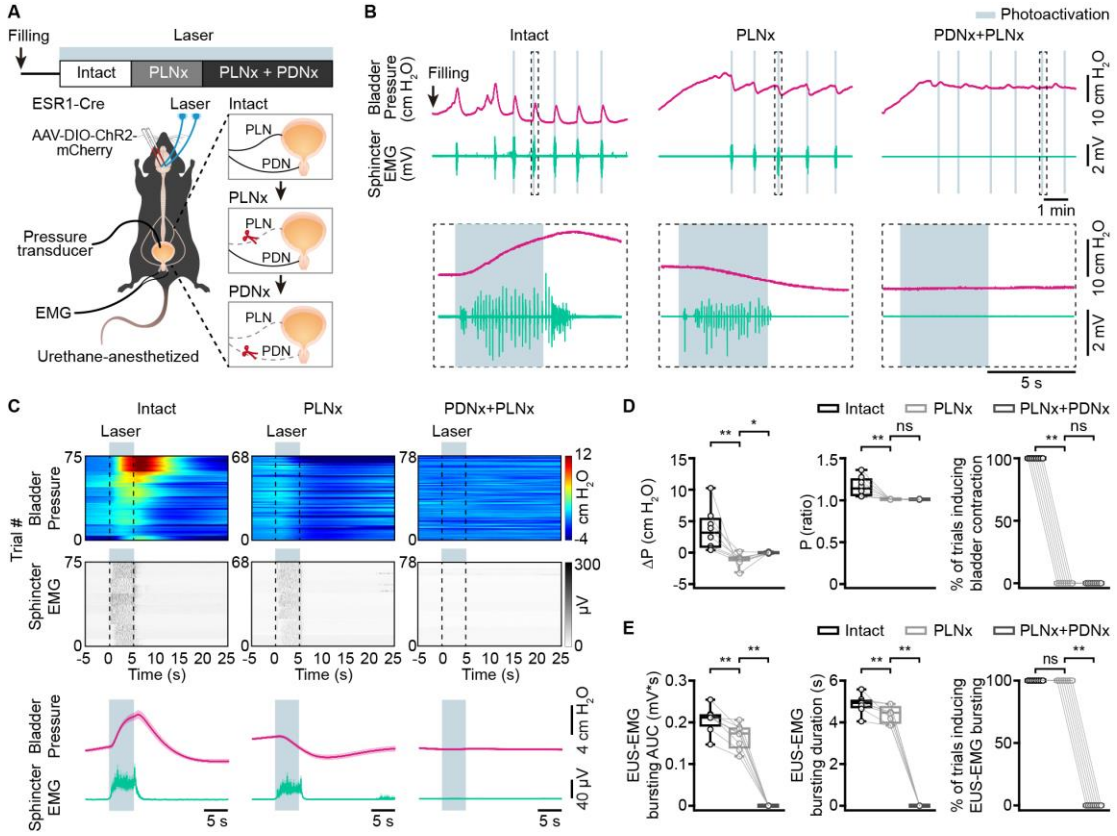

Figure 5. Transection of the pelvic nerves does not impair sphincter relaxation induced by PMC^{ESR1+} cell photoactivation.

(**A**) Timeline (top) and schematic (bottom) for PMC$^{ESR1\text{-}ChR2}$ photoactivation during simultaneous cystometry and urethral electromyography recordings, with PLNx performed first. PLNx, pelvic nerve transection; PDNx, pudendal nerve transection. (**B**) Representative traces (top) and expanded portions (bottom, from the dashed box in the top panel) showing bladder pressure (magenta) and EUS-EMG (teal) during PMC$^{ESR1\text{-}ChR2}$ photoactivation in various groups, with PLNx performed first. (**C**) Heatmap (top) and average traces (bottom; thick lines and shading represent mean ± s.e.m.) of sorted bladder pressure and EUS-EMG around photoactivation timepoint for all filled bladder trials with the PLNx-first experiment (n = 8 mice per group). (**D**) Quantification of bladder pressure parameters for the PLNx-first experiment from **c**: bladder pressure change (ΔP, left), bladder pressure ratio (middle), and the percentage of photoactivation-associated bladder contraction (right; from left to right: $^{**}P$ = 7.8e-3, P = 0.02, $^{**}P$ = 7.8e-3, P = 0.6, $^{**}P$ = 7.8e-3, P = 1, respectively; n.s., not significant; Wilcoxon signed-rank test). (**E**) Quantification of EUS-EMG parameters for the PLNx-first experiment from **c**: EUS-EMG bursting AUC (left), EUS-EMG bursting duration (middle), and the percentage of photoactivation-associated EUS-EMG bursting (right; from left to right: $^{**}P$ = 7.8e-3, $^{**}P$ = 7.8e-3, $^{**}P$ = 7.8e-3, $^{**}P$ = 7.8e-3, P = 1, $^{**}P$ = 7.8e-3,

950 respectively; n.s., not significant; Wilcoxon signed-rank test). For all data points in (**D, E**),
951 whisker-box plots indicate the median with the 25%-75% percentile as the box, and whiskers
952 represent the minimum and maximum values.

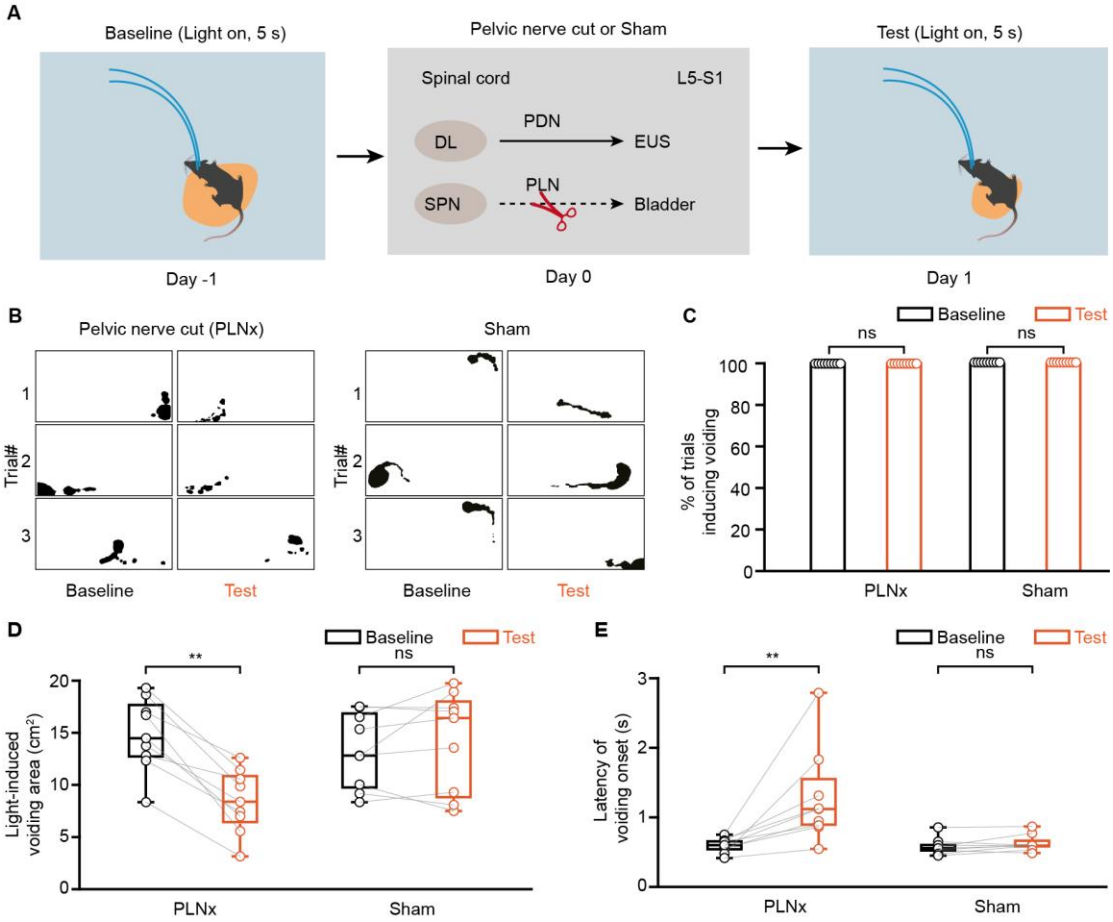

Figure 6. Transection of the pelvic nerves decreases urinary volume induced by PMC^{ESR1+} cell photoactivation.

(**A**) Schematic (top) and timeline (bottom) for PMC$^{ESR1\text{-}ChR2}$ photoactivation during simultaneous cystometry and urethral electromyography recordings in a freely moving mouse with pelvic nerve transection (PLNx). (**B**) Representative images of light-induced urination marking (black shading) in ESR1-Cre mice before ('Baseline') and after ('Test') pelvic nerve transection (left) or sham transection (right). (**C-E**) Quantification of the effect of pelvic nerve transection on voiding in the PLNx (n = 9 mice) and sham groups (n = 9 mice): the percentage of light-induced voiding (**c**, P = 1; n.s., not significant; Wilcoxon signed-rank test), light-induced voiding area (**D**, $^{**}P$ = 3.9e-3, P = 0.5, respectively), and latency of voiding onset after light stimulation (**E**, $^{**}P$ = 3.9e-3, P = 0.2, respectively; n.s., not significant; Wilcoxon signed-rank test). For all data points in (**D**, **E**), whisker-box plots indicate the median with the 25%-75% percentile as the box, and whiskers represent the minimum and maximum values.

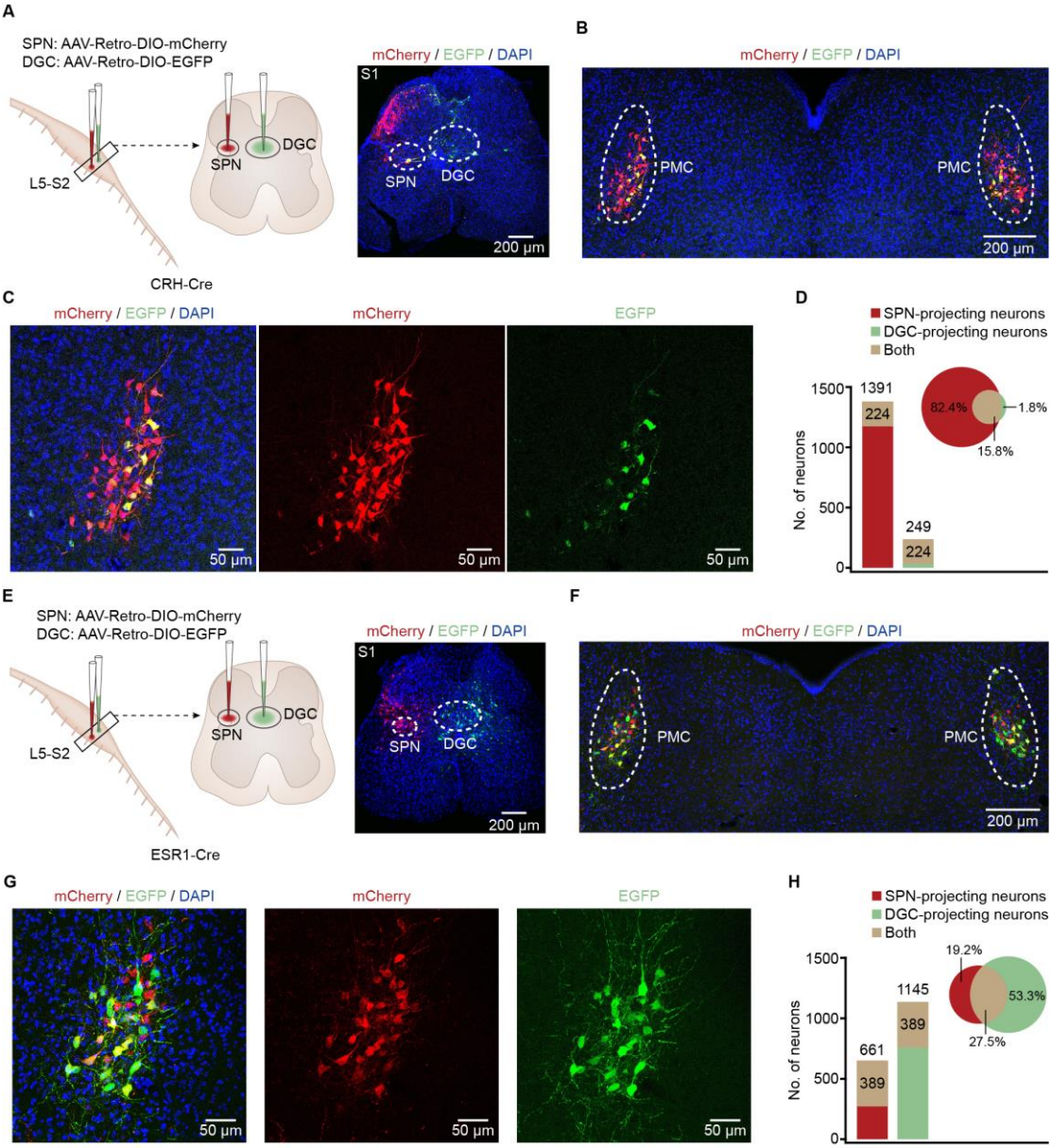

968

969 **Figure 7. Differences in the anatomical projections to the lumbosacral spinal cord between**
970 **PMC^{CRH+} and PMC^{ESR1+} cells.**

971 (**A**) Schematic of labeling (left) and representation histology of virus expression (right) at the
972 spinal cord of CRH-Cre mice. Scale bar: 200 µm. (**B, C**) Representative image (**B**) and enlarged
973 images (**C**, from the left part of **B**) showing EGFP and mCherry expression in the PMC of a
974 CRH-Cre mouse. Scale bars: 200 µm for (**B**) and 50 µm for (**C**). (**D**) Quantification of the
975 fractions of CRH^{+} cells specifically projecting to the SPN and DGC of the spinal cord,
976 respectively (n = 1416 cells from 3 mice). (**E**) Schematics of labeling (left) and representative
977 histology of virus expression (right) in the spinal cord of ESR1-Cre mice. Scale bar: 200 µm. (**F,**
978 **G**) Representative image (**F**) and enlarged images (**G**, from the left part of **F**) showing EGFP
979 and mCherry expression in the PMC of an ESR1-Cre mouse. Scale bars: 200 µm for (**F**) and 50

980 μm for (**G**). (**H**) Quantification of the fractions of ESR1^{+} cells specifically projecting to the SPN
981 and DGC of the spinal cord, respectively (n = 1417 cells from 5 mice). SPN, sacral
982 parasympathetic nucleus; DGC, dorsal gray commissure.

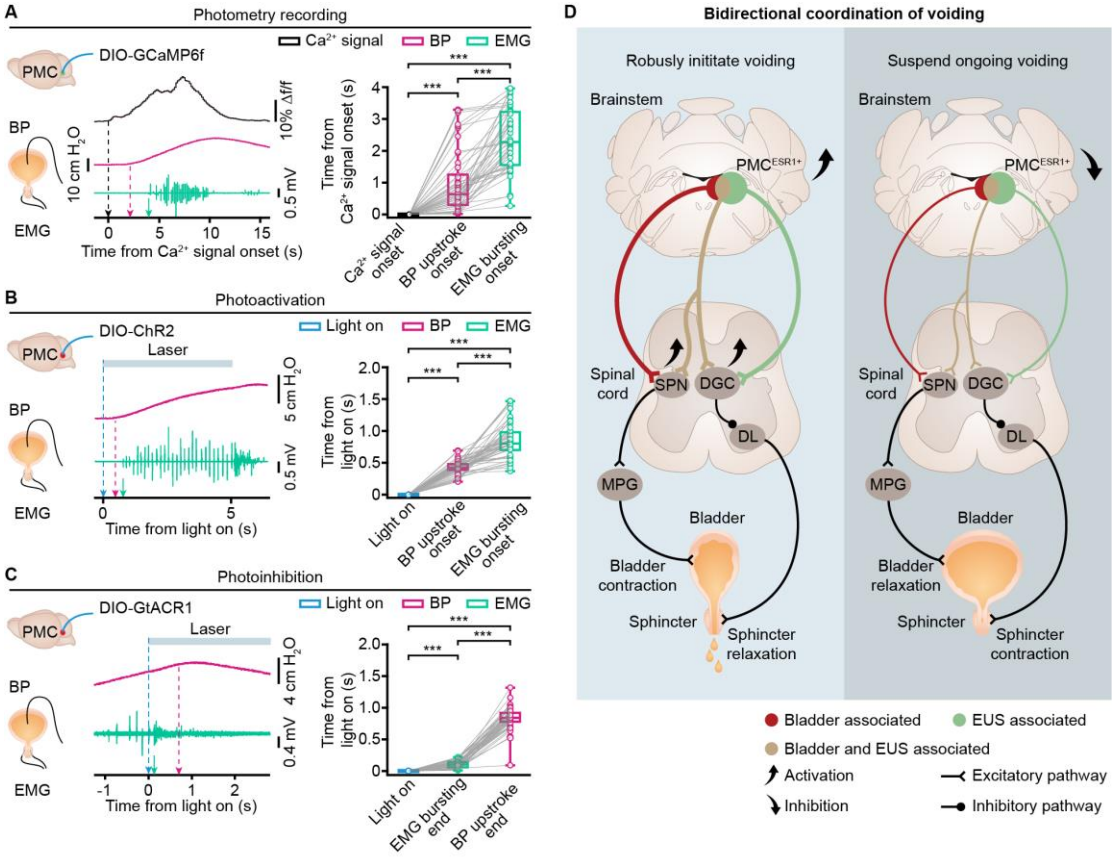

Figure 8. Coordination of bladder contraction and sphincter relaxation for urination by PMC^{ESR1+} cells.

(**A**) Left: Example (left, with arrows indicating the onset timepoints) and quantification (right) of the temporal relationships among the onset times of Ca^{2+} signals, bladder pressure (BP) upstroke, and EUS-EMG bursting in photometry recordings (n = 46 trials from 8 mice; Ca^{2+} signals onset, 0\0-0 s; BP upstroke onset, 0.6\0.3-1.2 s; EUS-EMG bursting onset, 2.3\1.5-3.2 s; ***P = 3.5e-9 for all, Wilcoxon signed-rank test). (**B**) Example (left, with arrows indicating the onset timepoints) and quantification (right) of the temporal relationships among the onset times of light stimulation, bladder pressure upstroke, and EUS-EMG bursting for the photoactivation group (n = 50 trials from 10 mice; Light on, 0\0-0 s; BP upstroke onset, 0.4\0.4-0.5 s; EUS-EMG bursting onset, 0.8\0.7-1.0 s; ***P = 7.6e-10 for all, Wilcoxon signed-rank test). (**C**) Example (left, with arrows indicating the onset timepoints) and quantification (right) of the temporal relationships among the onset time of light, EUS-EMG bursting end, and bladder pressure upstroke end for the photoinhibition group (n = 44 trials from 8 mice; Light on, 0\0-0 s; EUS-EMG bursting end, 0.1\0.1-0.2 s; BP upstroke end, 0.8\0.8-0.9 s; ***P = 7.6e-9 for all, Wilcoxon signed-rank test). (**D**) A working model of the brainstem-spinal compound circuit for bidirectional and coordinated control of voiding. Abbreviations: SPN, sacral parasympathetic nucleus; DGC, dorsal gray commissure; DL, dorsolateral nucleus;

1002 MPG, major pelvic ganglia. For all data points in (**A, B**), and (**C**), whisker-box plots indicate
1003 the median with the 25%-75% percentile as the box, and whiskers represent the minimum
1004 and maximum values.
1005

1006 **Figures supplement**

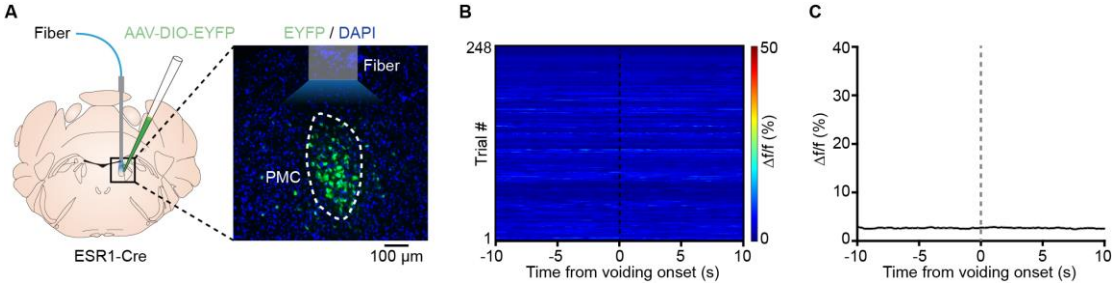

1007

1008 **Figure supplement 1. No change in fluorescence responses of EYFP-labeled PMC^{ESR1+} cells**

1009 **during voiding.**

1010 (**A**) Schematics of labeling (left) and representative histology (right) of PMC^{ESR1+} cells labeled with

1011 EYFP. Scale bar, 100 µm. (**B**) Cumulative sessions of fluorescence responses aligned to voiding

1012 onset (n = 248 trials from 9 mice). (**C**) Average fluorescence traces of PMC$^{ESR1-EYFP}$ aligned to

1013 voiding onset. The black line and shading represent mean ± s.e.m., respectively.

1014

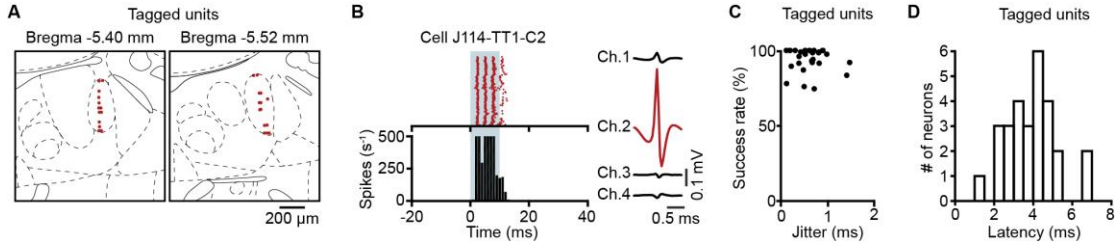

Figure supplement 2. Identification of recorded PMC^{ESR1+} cells in optrode recordings. (**A**) Tetrode locations for all recorded PMC^{ESR1+} units (red dots, n = 28 units from 4 mice). (**B**) Left: Raster plots (top) and histograms (bottom) showing the firing patterns of representative PMC$^{ESR1\text{-}ChR2}$ units upon optical stimulation at a power of 10 mW. Right: Waveforms of light-induced spikes from the unit shown on the left. (**C**) Comparison of success rates and temporal jitter for the first light-induced spike in all recorded PMC^{ESR1+} units. (**D**) Latency distribution for all recorded PMC^{ESR1+} units.

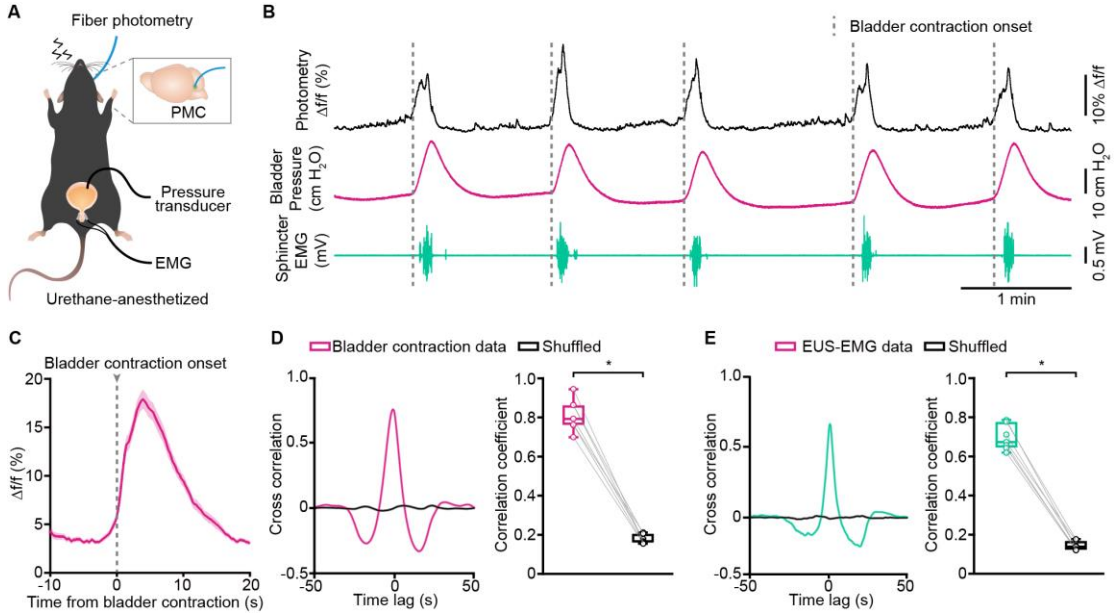

Figure supplement 3. The activity of PMC^{ESR1+} cells correlates with bladder contraction and sphincter relaxation.

(**A**) Schematic of fiber photometry recording for PMC^{ESR1+} cells during simultaneous cystometry and urethral electromyography in a urethane-anesthetized mouse. (**B**) Representative traces showing Ca^{2+} transients (black), bladder pressure (magenta), and EUS-EMG (teal) during fiber photometry recordings, with dashed lines indicating bladder contraction onset. (**C**) Average Ca^{2+} signals during bladder contraction from all trials (n = 101 trials from 7 mice). The thick line and shading represent mean ± s.e.m., respectively. (**D**) Cross-correlation (left) and correlation coefficients (right) between Ca^{2+} signals and bladder contraction events compared to shuffled data (n = 7 mice, $^{*}P$ = 0.02, Wilcoxon signed-rank test). (**E**) Cross-correlation (left) and correlation coefficients (right) between Ca^{2+} signals and EUS-EMG bursting events compared to shuffled data (n = 7 mice, $^{*}P$ = 0.02, Wilcoxon signed-rank test). For all data points in (**D, E**), whisker-box plots indicate the median with the 25%-75% percentile as the box, and whiskers represent the minimum and maximum values.

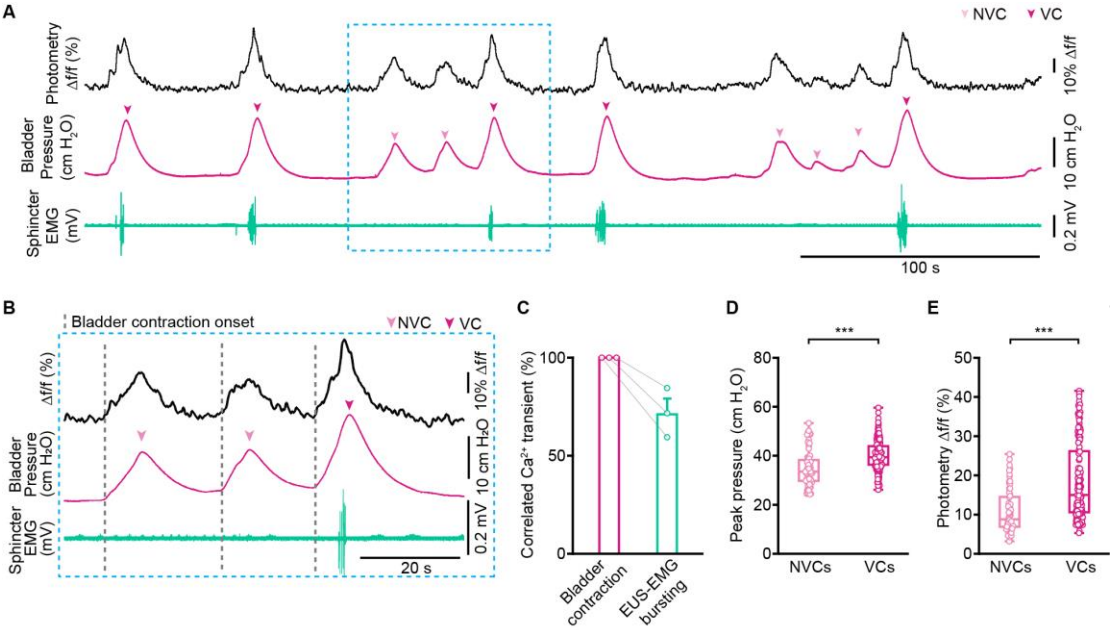

Figure supplement 4. No voiding contractions (NVCs) correlate with Ca^{2+} signals of PMC^{ESR1+} cells.

(**A**) Representative traces of Ca^{2+} transients (black), bladder pressure (magenta), and EUS-EMG (teal) for no voiding contractions (NVCs) and voiding contractions (VCs). (**B**) Expanded portions of no voiding contractions (NVCs, light magenta arrow) and voiding contractions (VC, dark magenta arrow) from (**A**) (blue dashed box). (**C**) Correlation rate of Ca^{2+} transient with bladder contraction and EUS-EMG bursting events (n = 3 mice per group). (**D, E**) Comparison of peak bladder pressure (**D**) and the amplitude of Ca^{2+} transients (**E**) between NVCs and VCs (NVCs: n = 62 events from 3 mice, VCs: n = 167 events from 3 mice; ***P = 6.03e-7, ***P = 6.8e-9, respectively, Wilcoxon rank-sum test). For all data points in (**D, E**), whisker-box plots indicate the median with the 25%-75% percentile as the box, and whiskers represent the minimum and maximum values.

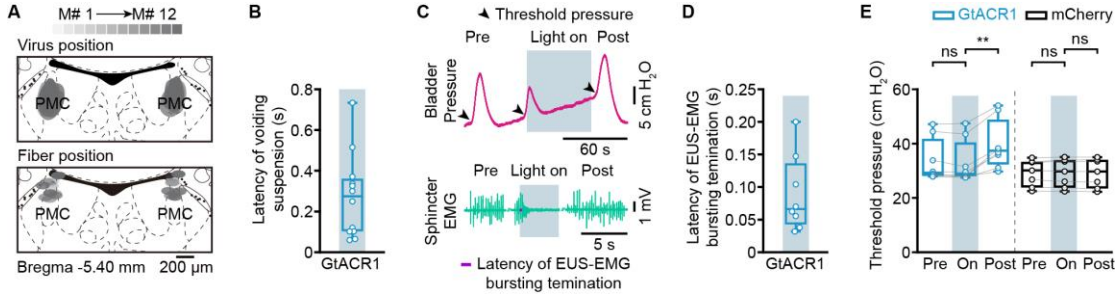

Figure supplement 5. Acute photoinhibition (60 s) of PMC^{ESR1+} cells operates the bladder and sphincter to suspend voiding, related to Figure 2.

(**A**) Overlay of viral expression areas (top) and fiber positions (bottom) from ESR1-Cre mice labeled with GtACR1 (n = 12 mice). (**B**) Latency of voiding suspension after light activation. (**C**) Representative raw traces of bladder pressure and EUS-EMG. (**D**) Latency of sphincter bursting termination after light activation (n = 8 mice). (**E**) Bladder threshold pressure during voiding before ('Pre'), during ('On'), and after ('Post') photoinhibition in PMC$^{ESR1\text{-}GtACR1}$ (n = 8 mice) and PMC$^{ESR1\text{-}mCherry}$ (n = 7 mice) groups (from left to right: P = 0.06, $^{**}P$ = 7.8e-3, P = 0.9, P = 0.4, respectively; n.s., not significant; Wilcoxon signed-rank test). For all data points in (**B, D**) and (**E**), whisker-box plots indicate the median with the 25%-75% percentile as the box, and whiskers represent the minimum and maximum values.

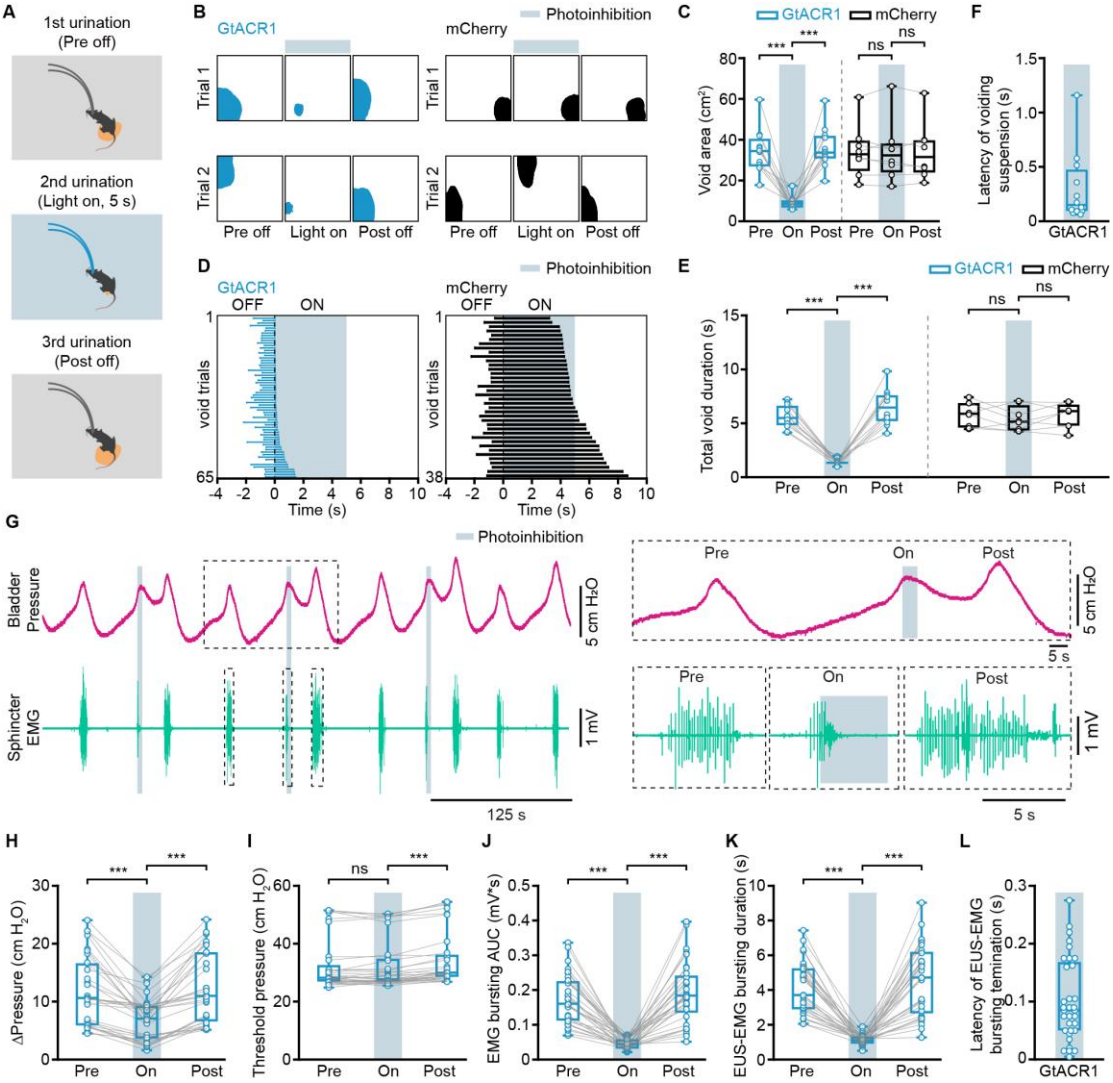

Figure supplement 6. 5-s photoinhibition of PMC^{ESR1+} cells suppresses bladder contraction and sphincter relaxation to suspend ongoing voiding.

(**A**) Experimental design for 5 s photoinhibition of PMC^{ESR1+} cells in a freely moving mouse. (**B, C**) Representative images (**B**, blue and black shading) and quantification (**C**) of the void area before, during, and after 5 s photoinhibition in PMC$^{ESR1\text{-}GtACR1}$ (n = 12 mice) and PMC$^{ESR1\text{-}mCherry}$ (n = 8 mice) groups (from left to right: ***P = 4.9e-4, ***P = 4.9e-4, P = 0.7, P = 0.9, respectively; n.s., not significant; Wilcoxon signed-rank test). (**D**) Cumulative trials of voiding duration during 5 s photoinhibition in PMC$^{ESR1\text{-}GtACR1}$ (blue bar, n = 65 trials from 12 mice) and PMC$^{ESR1\text{-}mCherry}$ groups (black bar, n = 38 trials from 8 mice), ordered by increasing voiding epoch time with the laser on. (**E**) Voiding duration before, during, and after 5 s photoinhibition in PMC$^{ESR1\text{-}GtACR1}$ (n = 12 mice) and PMC$^{ESR1\text{-}mCherry}$ (n = 8 mice) groups (from left to right: ***P = 4.9e-4, ***P = 4.9e-4, P = 0.3, P = 0.4, respectively; n.s., not significant; Wilcoxon signed-rank test). (**F**) Latency of urination suspension after light activation. (**G**)

1081 Representative traces (left) and expanded portions (right, from the dashed box in the left
1082 panel) of bladder pressure (magenta) and EUS-EMG (teal) before, during, and after 5 s
1083 photoinhibition in $PMC^{ESR1\text{-}GtACR1}$ individual. (**H-L**) Quantification of the effect of 5 s
1084 photoinhibition (n = 33 trials from 6 mice) on bladder pressure and EUS-EMG: Δpressure (**H**,
1085 $^{***}P$ = 5.4e-7), threshold pressure (**I**, P = 0.98, $^{***}P$ = 1.9e-6, respectively), EUS-EMG
1086 bursting AUC (**J**, $^{***}P$ = 5.4e-7), and EUS-EMG bursting duration (**K**, $^{***}P$ = 5.4e-7; n.s., not
1087 significant; Wilcoxon signed-rank test). (**L**) Latency of sphincter bursting termination after 5 s
1088 photoinhibition. For all data points in (**C**), (**E**), (**F**), and (**H-L**), whisker-box plots indicate the
1089 median with the 25%-75% percentile as the box, and whiskers represent the minimum and
1090 maximum values.
1091

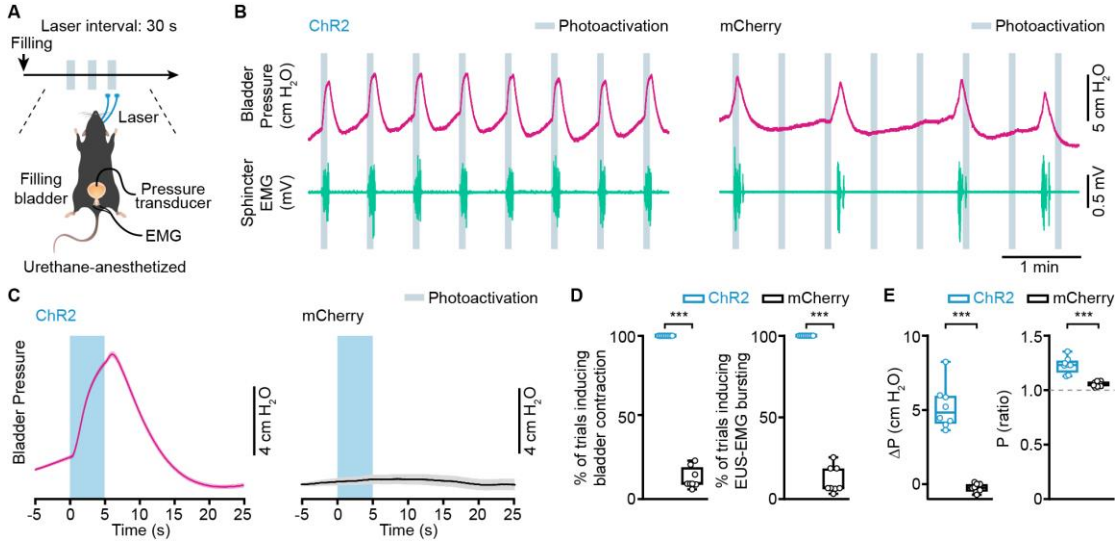

Figure supplement 7. Regular interval photoactivation of PMC^{ESR1+} cells induces both bladder contraction and external urethral sphincter relaxation.

(**A**) Timeline (top) and schematic (bottom) for regular interval photoactivation of PMC^{ESR1+} cells during simultaneous cystometry and urethral electromyography recording with a filled bladder. (**B**) Representative raw traces of bladder pressure (magenta) and EUS-EMG (teal) around the photoactivation timepoint in PMC$^{ESR1\text{-}ChR2}$ (left) and PMC$^{ESR1\text{-}mCherry}$ (right) individuals. (**C**) Average bladder pressure around photoactivation in PMC$^{ESR1\text{-}ChR2}$ (left, n = 8 mice) and PMC$^{ESR1\text{-}mCherry}$ (right, n = 8 mice) groups. The thick line and shading represent mean ± s.e.m., respectively. (**D, E**) Quantification of the photoactivation effect on the bladder detrusor and urethra sphincter in PMC$^{ESR1\text{-}ChR2}$ (n = 8 mice) or PMC$^{ESR1\text{-}mCherry}$ (n = 8 mice) groups: the percentage of bladder contraction (**D**, left), the percentage of EUS-EMG bursting (**D**, right), Δpressure (**E**, left), and bladder pressure ratio (**E**, right; ***P = 1.6e-4 for **D** and **E**, Wilcoxon rank-sum test). For all data points in (**D**, **E**), whisker-box plots indicate the median with the 25%-75% percentile as the box, and whiskers represent the minimum and maximum values.

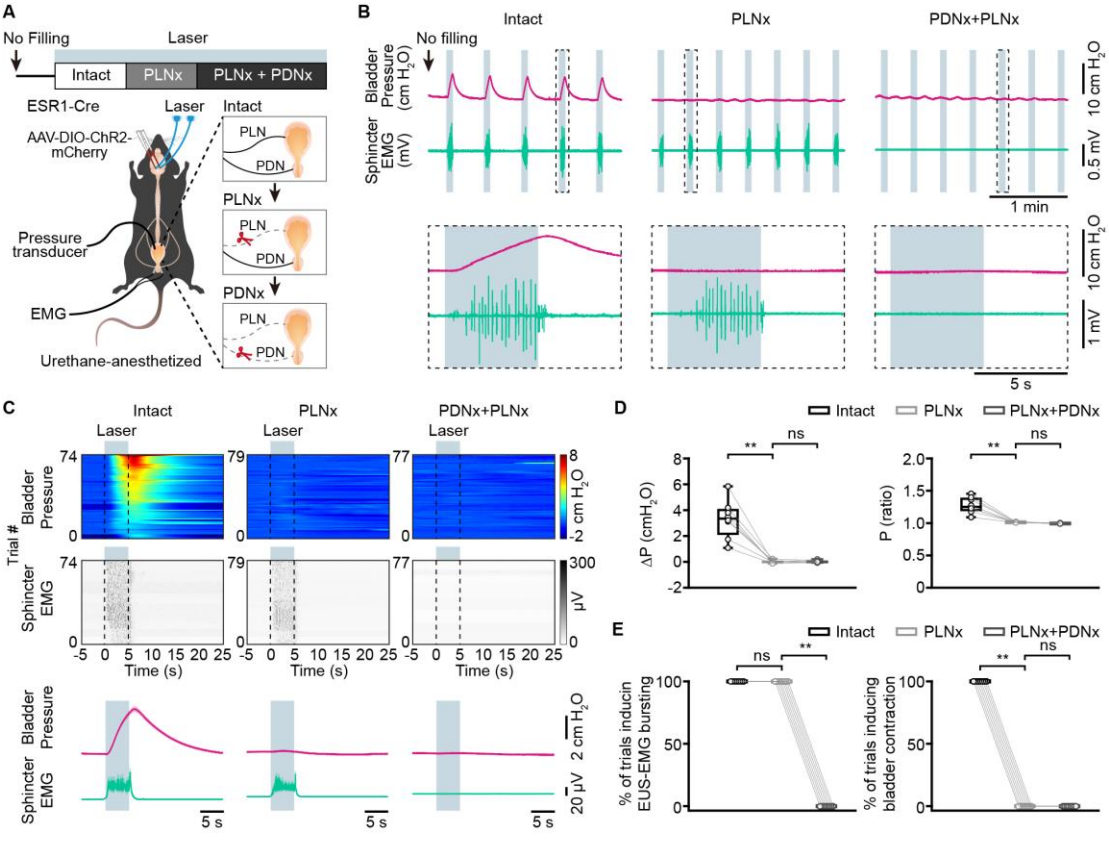

Figure supplement 8. Transection of the pelvic nerves does not alter bladder pressure in an unfilled bladder during PMC$^{ESR1\text{-}ChR2}$ photoactivation.

(**A**) Timeline (top) and schematic (bottom) for PMC$^{ESR1\text{-}ChR2}$ photoactivation during simultaneous cystometry and urethral electromyography recordings in a non-filled bladder, with PLNX performed first. PLNx: pelvic nerve transection; PDNx: pudendal nerve transection. (**B**) Representative traces (top) and expanded portions (bottom, from the dashed box in the top panel) showing bladder pressure (magenta) and EUS-EMG (teal) during PMC$^{ESR1\text{-}ChR2}$ photoactivation in an unfilled bladder with PLNX performed first. (**C**) Heatmap (top) and average traces (bottom, thick line, and shading represent mean ± s.e.m., respectively) of sorted bladder pressure and EUS-EMG around photoactivation timepoint for all unfilled bladder trials with PLNX performed first (*n* = 8 mice per group). (**D, E**) Quantification of bladder pressure change (ΔP, **D**, left), bladder pressure ratio (**D**, right), the percentage of photoactivation-associated bladder contraction (**E**, left), and the percentage of photoactivation-associated EUS-EMG bursting (**E**, right) upon photoactivation for the PLNx-first experiment from **C** (*n* = 8 mice per group, from left to right, **D**: $^{**}P$ = 7.8e-3, *P* =0.8, $^{**}P$ = 7.8e-3, *P* = 0.1, respectively; **E**: *P* = 1, $^{**}P$ = 7.8e-3, $^{**}P$ = 7.8e-3, *P* = 1, respectively; n.s., not significant; Wilcoxon signed-rank test). For all data points in (**D, E**) whisker-box plots indicate the median with the 25%-75% percentile as the box, and whiskers represent the

minimum and maximum values.

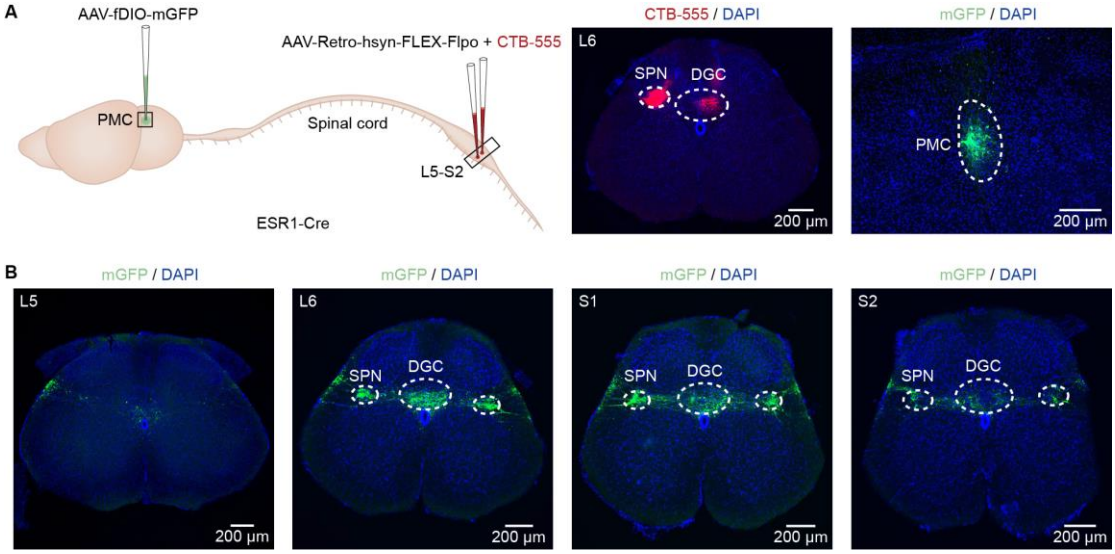

Figure supplement 9. PMC^{ESR1+} cells projection to the SPN and DGC in the spinal cord.

(**A**) Left: Schematic of labeling. Middle and right: Representative histological images showing CTB-555 expression in the lumbosacral spinal cord (middle) and mGFP expression in the PMC (right). Scale bars: 200 µm. (**B**) Axonal projections of PMC$^{ESR1\text{-}mGFP}$ cells in the lumbosacral spinal cord from L5 to S2 levels (n = 3 mice). Scale bars: 200 µm. Abbreviations: SPN, sacral parasympathetic nucleus; DGC, dorsal gray commissure.